A COMPUTATIONAL FLUID DYNAMICS INVESTIGATION OF MOTION MITIGATION ON A FLOATING OBJECT CONTAINING TUNED LIQUID COLUMN DAMPER

A Thesis Submitted to
the Graduate School of
İzmir Institute of Technology
in Partial Fulfillment of the Requirements for the Degree of

MASTER OF SCIENCE

in Mechanical Engineering

by
Ramazan Kadir ZENGİN

July 2024
İZMİR

We approve the thesis of **Ramazan Kadir ZENGİN**

Examining Committee Members:

Assoc. Prof. Dr. Ünver ÖZKOL

Department of Mechanical Engineering, İzmir Institute of Technology

---

Prof. Dr. Erdal ÇETKİN

Department of Mechanical Engineering, İzmir Institute of Technology

---

Assoc. Prof. Dr. Utku ŞENTÜRK

Department of Mechanical Engineering, Ege University

12 July 2024

Assoc. Prof. Dr. Ünver ÖZKOL

Supervisor, Department of
Mechanical Engineering, İzmir
Institute of Technology

Prof. Dr. M. İ. Can DEDE

Head of the Department of
Mechanical Engineering

Prof. Dr. Mehtap EANES

Dean of the Graduate School

ACKNOWLEDGMENTS

First and foremost, I would like to express my deepest thanks to my advisor, Assoc. Prof. Dr. Ünver ÖZKOL for his encouragement, support, and patience throughout this study. Throughout my thesis research, he has been an excellent mentor, offering insightful advice and motivating me to pursue further knowledge.

Secondly, thanks to The Scientific and Technological Research Council of Türkiye (TUBITAK) ULAKBIM. The numerical calculations reported in this thesis paper were performed at TUBITAK ULAKBIM, High Performance and Grid Computing Center (TRUBA HPC resources).

Finally, I would like to express my sincere thanks to my parents and sisters for their constant encouragement and kindness throughout my whole life.

ABSTRACT

A COMPUTATIONAL FLUID DYNAMICS INVESTIGATION OF MOTION MITIGATION ON A FLOATING OBJECT CONTAINING TUNED LIQUID COLUMN DAMPER

The global shift towards net-zero emission energy systems has heightened interest in sustainable developments and renewable energy alternatives, with wind emerging as a key resource. However, conventional methods struggle to access wind resources in deepwater areas. Floating Offshore Wind Turbines (FOWTs) have overcome this limitation, enabling the harnessing of wind energy at previously inaccessible deep-water sites. To extend the operational life of FOWTs, it is crucial to minimize undesirable loads and motions.

This project investigates a methodology for high-fidelity, coupled simulation of FOWTs in OpenFOAM. The waves2Foam tool by (Jacobsen et al. 2012), utilizing the relaxation zone method, is employed for wave generation and absorption, while mooring restraints are computed using a quasi-steady catenary model. The multiphase simulation employs the waveDyMFoam solver, modified by the interFoam solver, incorporating dynamic mesh techniques. Fluid-structure interaction (FSI) coupling is implemented through a PIMPLE-based, serial sub-iterating strategy. The methodology was developed incrementally, beginning with the Tuned Liquid Column Damper (TLCD) implementation, validated against existing studies. Free-decay analysis was then conducted on a wave energy converter (WEC), confirming the damping performance of a TLCD applied with varying mass ratios. Eventually, motion mitigation was obtained in free decay condition by 47.80% with a 4% mass ratio TLCD application and 37.01% achieved under regular wave conditions.

The methodology successfully demonstrates the damping performance of TLCD and Tuned Liquid Multi Column Damper (TLMCD) applications on floating objects under wave conditions, making it a reliable technique for TLMCDs in FOWT modeling.

ÖZET

YÜZER BİR CİSMİN AYARLI SIVI KOLON DAMPERİ İLE HAREKET AZALMA PERFORMANSININ HESAPLAMALI AKIŞKANLAR DİNAMİĞİ YÖNTEMİ İLE İNCELENMESİ

Net sıfır emisyon enerji sistemlerine yönelik küresel dönüşüm, sürdürülebilir gelişmelere ve yenilenebilir enerji alternatiflerine olan ilgiyi artırmış, rüzgâr bu bağlamda ön plana çıkmıştır. Ancak, geleneksel yöntemler derin su bölgelerindeki rüzgâr kaynaklarına erişimde zorlanmaktadır. Denizüstü Yüzer Rüzgar Türbinleri (YRT), bu engeli aşarak daha önce erişilemeyen derin su sahalarından rüzgâr enerjisi elde etmeyi mümkün kılmıştır. YRT'lerin ömrünü uzatmak için istenmeyen yük ve hareketlerin en aza indirilmesi kritik öneme sahiptir.

Bu proje, OpenFOAM kullanarak YRT'lerin yüksek doğruluklu ve entegre bir simülasyon metodolojisini araştırmaktadır. Dalga üretimi ve sönümlemesi için "sönümleme bölgesi" yöntemini kullanan waves2Foam aracı (Jacobsen et al. 2012) kullanılmış ve demirleme kuvvetleri yarı sabit katener modeli ile hesaplanmıştır. Çok fazlı simülasyon, dinamik ağ teknikleri entegre edilen waveDyMFoam çözücüsü ile gerçekleştirilmiştir. Akışkan-Yapı Etkileşimi (AYE) bağlantısı, PIMPLE metoduna dayalı, seri alt yineleme stratejisi ile sağlanmıştır. Metodoloji, Ayarlanmış Sıvı Kolon Sönümleyici (ASKS) uygulaması ile adım adım geliştirilmiş ve mevcut çalışmalarla doğrulanmıştır. Ardından, bir Dalga Enerji Dönüştürücüsü (DED) üzerinde serbest bozunma analizi yapılmış ve ASKS'nin farklı kütle oranları altında sönümleme performansı doğrulanmıştır. Serbest bozunma koşullarında %4 kütle oranlı ASKS uygulaması ile hareket azaltımı %47,80, düzenli dalga koşullarında ise %37,01 olarak elde edilmiştir.

Bu metodoloji, ASKS ve Ayarlanmış Sıvı Çok Kolonlu Damper (ASÇKS) uygulamalarının dalga koşulları altında yüzer nesneler üzerindeki sönümleme performansını başarıyla göstermekte olup, YRT modellemesi için ASKS'nin güvenilir bir teknik olduğunu kanıtlamaktadır.

TABLE OF CONTENTS

LIST OF FIGURES viii

LIST OF TABLES x

CHAPTER 1. INTRODUCTION 1

1.1. A brief overview of FOWTs 2

1.1.1. Six-degrees of freedom 2

1.1.2. Classifications of FOWTs 4

1.1.3. The Tuned Liquid Column dampers (TLCD) 5

1.1.4. Mooring lines 7

1.2. The Structure of the Thesis 7

CHAPTER 2. LITERATURE REVIEW 9

2.1. Simulation Methods for FOWT Platforms 10

CHAPTER 3. THEORY AND METHODOLOGY 13

3.1. Hydrodynamics of FOWTs 13

3.1.1. Description of Ocean Waves 13

3.1.1.1Wave Theories 15

3.1.1.2Linear Waves 15

3.1.1.3Non-Linear Waves 17

3.1.2. Hydrostatic Behavior of FOWTs 18

3.1.3. Wave-Structure Interaction Loads 20

3.2. Computational Fluid Dynamics (CFD) 21

3.2.1. Multiphase Flow and the Volume of Fluid (VOF) Method 23

3.2.2. Dynamic Mesh Structures 24

3.2.3. Fluid-Structure Interaction (FSI) 26

3.2.4. Rigid Body Dynamics 26

3.3. OpenFOAM Environment and the Finite Volume Method (FVM) 28

3.3.1. Discretization of the Governing Equations 29
3.3.2. The PIMPLE Algorithm 29
3.3.2.1Pressure-velocity coupling 30
3.4. Numerical Wave Tank Implementation with The waves2foam Library and Relaxation Zone Method 31

CHAPTER 4. SIMULATIONS 35
4.1. Simulations of U-Shaped Anti Roll Tank with Prescribed Motion 35
4.1.1. Geometry and Grid 36
4.1.2. Initial and Boundary Conditions 38
4.1.3. Schemes and simulation controls 38
4.1.4. Results and Discussion 39
4.2. 3D Cylinder Simulations of Pitch Motion Decay (Free, Mooring and with TLMCD) 41
4.2.1. Geometry and Grid 42
4.2.2. Initial and Boundary Conditions 45
4.2.3. Schemes and simulation controls 47
4.2.4. Results and Discussion 47
4.3. 3D Cylinder Simulations of the Motion Under Regular Wave Conditions 50
4.3.1. Initial and Boundary Conditions 50
4.3.2. Results and Discussion 51

CHAPTER 5. CONCLUSIONS 54

REFERENCES 55

LIST OF FIGURES

Figure **Page**

Figure 1.1. Environmental Loads of FOWT 3
Figure 1.2. 6-DOF Definition of Semi-submersible FOWT 3
Figure 1.3. Main FOWT classes 4
Figure 1.4. Passive Tank U-Shaped ART System 6
Figure 1.5. TLMCD Applied FOWT Illustration 6
Figure 1.6. Mooring line types: catenary on the left, semi-taut (inclined tensioned/spread moorings) in the middle, and tensioned on the right. 7
Figure 3.1. Classifying the ocean wave spectrum according to wave period. 14
Figure 3.2. Definitions of sinusoidal, progressive wave, elementary wave terms. 16
Figure 3.3. Water particle trajectories in different depths 16
Figure 3.4. The comparison of the Pierson-Moskowitz spectrum and the standard JONSWAP spectrum. 17
Figure 3.5. Simplified Diagram of Metacenter and Metacentric Height 20
Figure 3.6. A visualization of how $\alpha_R(\chi_R)$ varies for the relaxation zones at the inlet and outlet. 32
Figure 3.7. Simplified diagram of the PIMPLE algorithm, reproduced by (Greenshields et al. 2022) and (Frontera Pericàs 2022) based on this thesis. 34
Figure 4.1. Schematic overview of U-shaped TLCD 36
Figure 4.2. ART mesh domain represented with α-water 1 represented red, α-air 0 represented blue, free surface 0.5 represented white with boundary conditions 37
Figure 4.3. ART mesh detail with boundary layer 38
Figure 4.4. Velocity at 9.2nd period. 39
Figure 4.5. Validation with experimental and CFD data 40
Figure 4.6. Vorticity at 9.4th period. 41
Figure 4.7. The Present Computational domain 43
Figure 4.8. Domain Scheme 44
Figure 4.9. Sliced mesh with refinement zones 45

Figure **Page**

Figure 4.10. Boundary layers around cylinder 45

Figure 4.11. Section cut of the computational domain of TLCD applied configuration with initial TLCD water level representations..... 46

Figure 4.12. The comparison of the pitch decay motion of the cylindrical floater with experimental and CFD data for both base-free configuration and moored configurations. 48

Figure 4.13. The comparison of the pitch decay motion of the cylindrical floater with base-free configuration, moored and TLCD applied configurations..... 49

Figure 4.14. Snapshot of hydrostatic pressure representation of entire domain. 51

Figure 4.15. (a) Entire computational domain showing the moored configuration of the floater with water level representation; (b) Close-up view of the floater with the same water level representation. 52

Figure 4.16. (a) Entire computational domain with 4% TLCD and mooring lines applied; (b) Close-up view of the floater with water level representation..... 53

Figure 4.17. Results from comparing the pitch decay motion of the cylindrical floater with base-free configuration, moored and TLCD applied configurations. 53

LIST OF TABLES

Table **Page**

Table 2.1. Explanation and abbreviations of computational methods used for FOWTs 9
Table 2.2. High-fidelity software for modelling FOWTs 10
Table 2.3. Summary of related studies. 11
Table 4.1. Essential details on full-scale ART and its physical components used in simulations. 37
Table 4.2. Masses for different TLCD configurations..... 43
Table 4.3. Numerical domain set-up dimensions and parameters of the floater and mooring line: draft d, mooring line length l_m, height h, inertia moment I_{xx}, center of gravity C_g, and density ρ_m. 44
Table 4.4. Comparison of pitch decay motion periods between experimental and CFD results for free,moored and TLCD applied configurations..... 49
Table 4.5. Regular waves (stream function) parameters..... 51

CHAPTER 1

INTRODUCTION

The growing global trend towards net-zero emission energy systems has led to increased interest in sustainability developments and the search for alternatives to renewable energy sources. Due to its high availability, wind energy is the first natural resource to be used.

Deepwater wind resources are difficult to reach through conventional methods; however, Floating Offshore Wind Turbines (FOWTs) are opened the possibility to overcome this barrier. It is expected that floating offshore wind energy will accelerate quickly starting in 2030, with 80% of the world's offshore wind resource potential located in regions with sea depths of more than 60 meters (GWEC 2023). FOWTs are seen as the wind technology of the future because the wind potential over the seas is higher than on land, the wind is less turbulent, and the acoustic and aesthetic side effects caused by its distance from human settlements are low. However, the performance of floating wind turbines depends on wind speed and direction as well as the movement of the platform on which they are placed, there's a price for this: the additional degrees of freedom on the platform create complicated aerodynamic and hydrodynamic behaviors, which require precise modeling to lower load uncertainties and eventually challenge the financial feasibility of FOWTs.

Since the FOWTs were developed 1990's, they took their current form as a result of numerous research and improvement efforts. Many methods are used in designing these systems, Computational Fluid Dynamics (CFD) methods are used for high-fidelity simulations, where dissolution of viscous dissipation is mandatory as in this study (Otter et al. 2022).

The Tuned Liquid Column dampers (TLCD), initially developed for naval and civil engineering applications, have been applied to minimize structural vibrations of buildings and ships (Gunsing et al. 2014; Balendra et al. 1999). Eventually, they have been used for FOWTs to mitigate the motion. Since reducing platform movement reduces fatigue amplitude, it also increases the lifespan of turbines (Hemmati et al. 2019; Coudurier et al. 2018).

The primary objective of the current research is to provide a simulation methodology that, at a reasonable computing cost, can accurately characterize the coupled FOWT system (TLCD applied platform + moorings). For this purpose, the relaxation zone method will be used for wave field generation, the Volume of Fluid (VOF) method will be used for multi-phase flow structure and the simulation framework will be constructed in OpenFOAM® open-source CFD environment.(Greenshields 2023)

The original aim of this thesis was to make simulations on the FOWTs platform's complex geometry to investigate motion mitigation. After having realized the complexity of the setup on the cluster and considering rather expensive computational resources, it became very clear that some additional foundational simulations were required to get proper and reliable results. My focus has therefore been oriented to the completion of a Wave Energy Converter (WEC) simulation, which is regarded as a basic preliminary step toward the attainment of an FOWTs analysis.

The successful completion of the WEC simulation proves that the methodology is capable not only of running complex computational tasks with OpenFOAM on an HPC cluster but also lays a very robust foundation for further work. While the full extent of FOWTs analysis was not quite realized within this thesis timeframe, progress made with the simulations of WEC will have valuable insights and set clear paths for further research.

1.1. A brief overview of FOWTs

This section gives brief information about floating offshore wind turbines' (FOWTs) loads, classifications of FOWTs platforms, the tuned liquid column dampers (TLCDs) and mooring lines.

1.1.1. Six-degrees of freedom

The environmental loads of waves, turbulent wind, currents, and ice impact are transferred through the foundations into the soil in conventional, bottom-fixed wind turbines. Although there are flexible deformations, these turbines are considered stationary since all of their rigid-body degrees of freedom (DOFs) are limited. Figure 1.1 shows environmental loads mostly seen. However, FOWTs load transfer into the soil is not ef-

fective as on-shore turbines. They do by mooring lines and anchors into the soil. Hence, they are vulnerable to motion in all six degrees of freedom (6-DOF). Three of translations

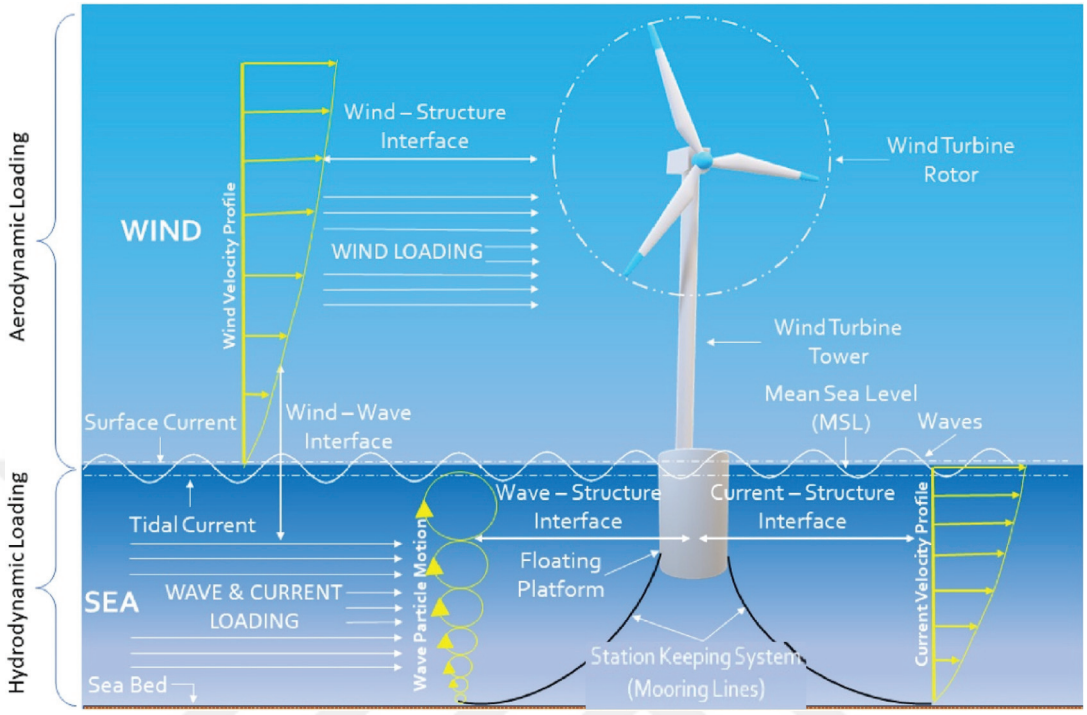

Figure 1.1. Environmental Loads of FOWT (Source: Clement et al. 2021)

(surge, sway, and heave) and other tree rotations (roll, pitch, and yaw) are shown in Figure 1.2. The modeling complexity rises with these additional degrees of freedom.

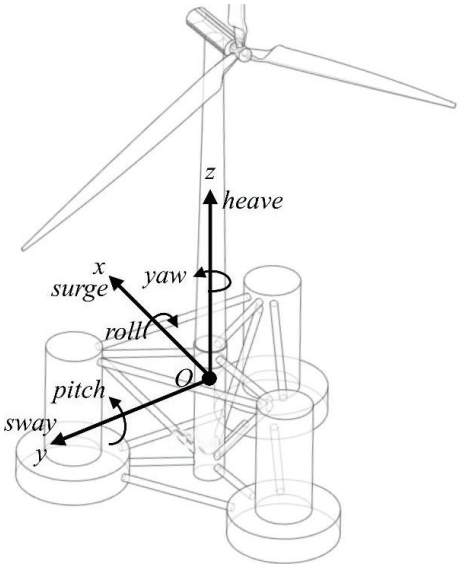

Figure 1.2. 6-DOF Definition of Semi-submersible FOWT (Source: Alkarem 2020)

1.1.2. Classifications of FOWTs

The oil and gas (O&G) industry is the source of technology used in offshore turbine support structures in the wind energy industry (Rodriguez Marijuan 2017). The two primary categories of support structures are bottom-fixed and floating platforms, which are adapted from several mobile and fixed drilling platforms utilized in the O&G industry. Figure 1.3 shows 4 main different platforms commonly used in the offshore wind industry:

Spar-buoy or ballast type: When a cylinder containing ballast in the lower section is moored to the seabed by catenary mooring lines, the center of gravity is lowered to be below the buoyancy center, providing stability. OC3-Hywind, Sway, and UMaine Spar FOWT platforms are examples of this type of platform (Robertson et al. 2011).

Tension leg platform (TLP) or mooring stabilized type: A shallow semi-submersible foundation holds the turbine in place, while tensioned mooring lines, vertically anchored to the bottom, provide stability. UMaine TLP, PelaStar, and Eco TLP are examples of TLP platforms (Frontera Pericàs 2022).

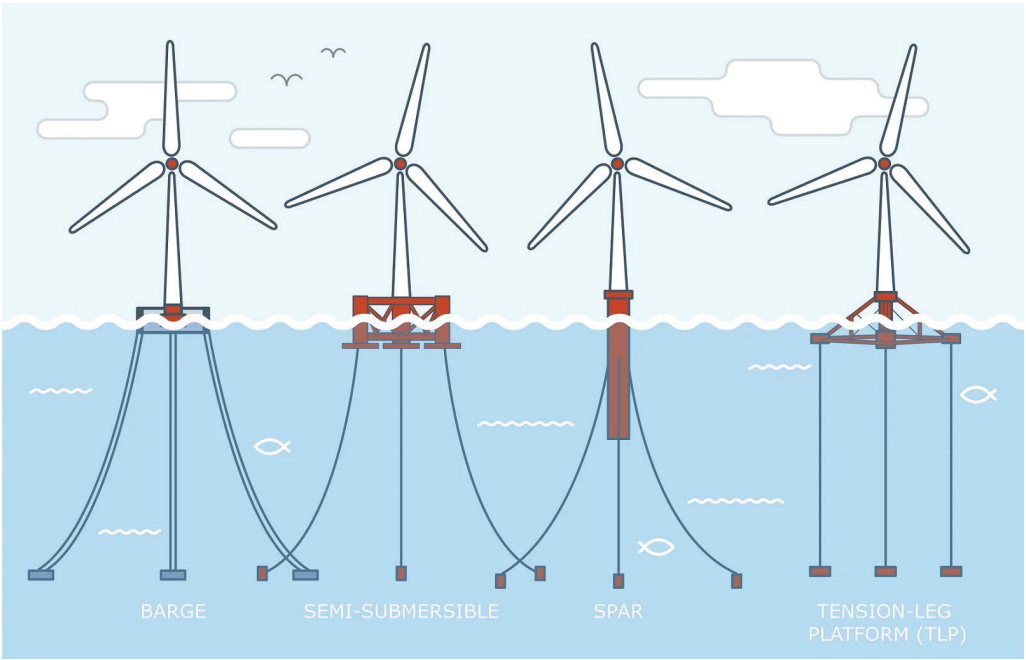

Figure 1.3. Main FOWT classes (Source: Erlend 2021)

Barge or waterplane type: Barge-type platforms provide stabilization with a short

draft and a large waterplane area. Catenary lines are utilized to prevent the platform from being pulled by the waves. However, compared to other platforms, the barge is less resistant to waves. Therefore, semi-submersibles are used more frequently at such sites (Robertson et al. 2011).

Semi-submersible: The structure, which consists of multiple cylinders, is anchored to the bottom by catenary mooring lines and floats partially submerged on the ocean's surface like a combined barge and spar. The columns are positioned vertically in the water. Compared to the barge, the equally spaced columns reduce the pitch and roll response. The additional buoyancy force is produced by the cylinders, and typically one of them supports the turbine (Arıdıcı 2022).

1.1.3. The Tuned Liquid Column dampers (TLCD)

FOWT structures are placed in challenging loads by the environmental conditions. Significant contributions were made by the naval and civil engineering studies to decrease six DOF motions and improve the lifespan of FOWTs.

Therefore, civil engineering studies on mitigating earthquakes and wind gusts affect skyscrapers, and for naval engineering ship roll motion mitigation has always been necessary to maintain since the steamboat era. To improve structural stability, tuned mass dampers (TMD) systems are effective by moving masses to the structure (Saaed et al. 2013). For cost-effective solutions for naval applications, tuned liquid column damper (TLCD) systems are invented. They are also known as the U-tank or Anti-roll tanks (ART) which were first mentioned by Frahm (Frahm 1911; Moaleji et al. 2007) for ship roll motion control, which basically U-shaped tubes are mostly filled with water and located a plane perpendicular to the roll axis of the ship. Figure 1.4 shows the motion cycles of the passive ART system.

Eventually, the TLCDs are the passive and semi-active structural control systems that are good alternatives for FOWTs structural control according to relatively new studies (Luo et al. 2011; Shadman et al. 2012; Coudurier et al. 2015). TLCDs are mostly used as The Tuned Liquid Multi Column Damper (TLMCD) which contains multiple columns filled by liquid for FOWT floating applications. Figure 1.5 shows illustration of TLMCD applied FOWT.

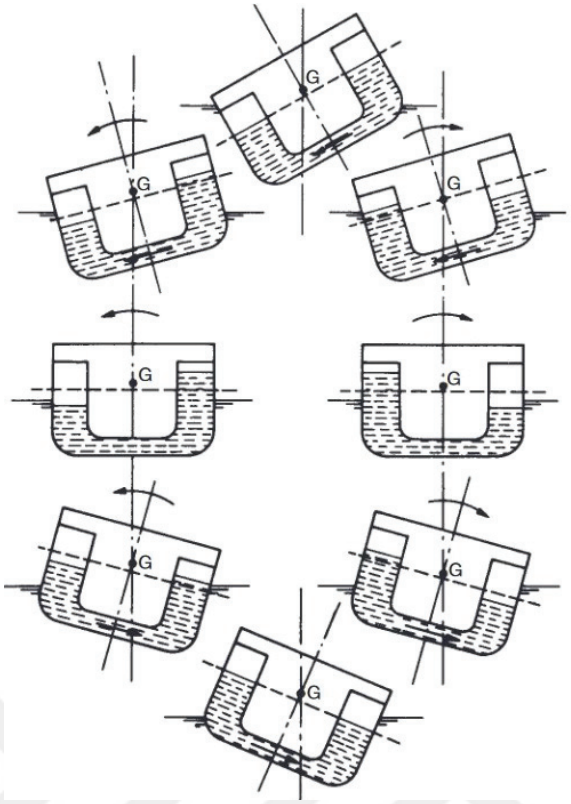

Figure 1.4. Passive Tank U-Shaped ART System (Source: Molland 2008)

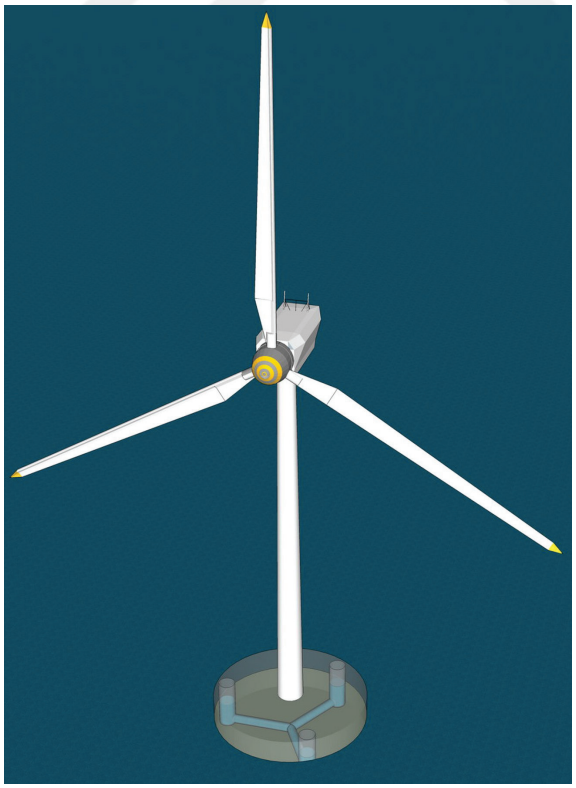

Figure 1.5. TLMCD Applied FOWT Illustration (Source: Coudurier et al. 2018)

1.1.4. Mooring lines

Mooring systems have been used for enabling floating structure operations in deep waters when traditional foundations are either technically or economically prohibitive. The combination of the buoyancy and mooring lines plays a key role in the structure maintain the position and orientation of FOWTs (Cruz et al. 2016). Through the fairleads, which direct their direction concerning the platform, the mooring lines are fastened to the platform. There are three types of mooring systems shown at Figure 1.6:

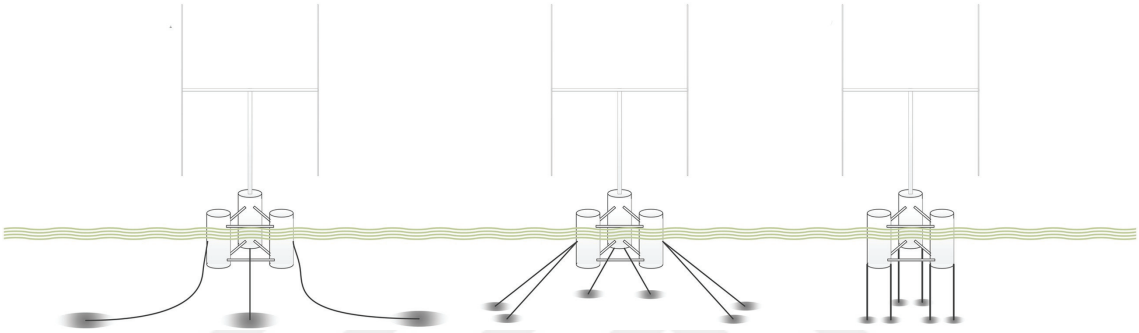

Figure 1.6. Mooring line types: catenary on the left, semi-taut (inclined tensioned/spread moorings) in the middle, and tensioned on the right. (Source: Borg et al. 2014)

Catenary: The chain lines or wires that freely fall from a floating surface platform to anchors on the seabed at a distance from the platform. The mooring line's mass and the anchor horizontal forces combine to preserve the platform's position by limiting the degrees of freedom for surge, sway, and yaw (Borg et al. 2014).

Semi-taut and Tensioned: Compared to the catenary type, this types produces restoring forces in each of the six DOF. The lightweight elastic lines and taut lines are connected inclined Fig. 1.6(b) and vertically Fig. 1.6(c) from seabed to the platform to maintain the platform position with elastic forces when the platform unsettled from its steady position (Borg et al. 2014).

1.2. The Structure of the Thesis

This section provided brief information about FOWTs and their components including TLCD and mooring line mechanisms. Chapter 2 focuses on related studies in

literature with their implementations and main findings which helped to design this thesis. Chapter 3 covers the overview of the essential concepts pertinent to the thesis, covering hydrodynamics fundamentals such as the stability of floating objects and wave propagation. It also includes an overview of Computational Fluid Dynamics (CFD), focusing on multi-phase flow, actuator models, and Fluid-Structure Interaction (FSI) with emphasis on rigid body coupling and dynamic mesh. The chapter concludes with an introduction to OpenFOAM. Chapter 4 investigates the FOWT motion reduction by CFD simulations, to achieve this purpose simulation steps are investigated including floating rigid bodies, employing dynamic mesh and FSI techniques. Chapter 5 summarizes the key findings and offers recommendations for future research.

CHAPTER 2

LITERATURE REVIEW

The increasing demand for sustainable power sources has given rise to the floating offshore wind turbines (FOWTs) industry in renewable energy. Sophisticated modeling approaches are essential to ensure both efficiency and feasibility, considering the specific constraints presented by the dynamic ocean environment. Numerical and physical (experimental) modeling approaches are being utilized for this purpose (Cruz et al. 2016).

Numerical modeling techniques, which we used in this thesis, for FOWTs can be divided into three categories: aerodynamics, hydrodynamics, and structural dynamics, mostly used methods are shown in Table 2.1.

Table 2.1. Explanation and abbreviations of computational methods used for FOWTs (Source: Otter et al. 2022)

Acronym	**Category**	**Fidelity**
CFD: Computational Fluid Dynamics	Aero-/hydrodynamic	High
BEM: Boundary Element Method	Hydrodynamic	Mid
BEMT: Blade Element Momentum Theory	Aerodynamic	Mid
Dyn: Dynamic method	Structural	Mid
ME: Morison Equation	Hydrodynamic	Mid
PF: Potential Flow	Aero-/hydrodynamic	Mid
FVW: Free Vortex Wake method	Aerodynamic	Mid
GDW: Generalized Dynamic Wake method	Aerodynamic	Mid
QS: Quasi-Static method	Structural	Low

The development of FOWTs requires numerical modeling, which comes in a variety of fidelity levels from low to high. For initial sizing and feasibility investigations, low-fidelity models like linear frequency-domain solvers are generally employed in the early phases of design. There are several examples of low fidelity models are developed for example, (Karimi et al. 2017; Pegalajar-Jurado et al. 2018) and (Hegseth et al. 2019).

Mid-fidelity models are used for more in-depth assessments, such as analyzing the global dynamics of FOWTs under various operating conditions. They provide a balance between computational efficiency and accuracy. The researchers use mid-fidelity

techniques to model the dynamic behavior of the DeepCwind semisubmersible FOWT in the OC4, OC5, and OC6 projects, and a spar FOWT design comparable to Hywind in the OC3 and OC4 projects (Robertson et al. 2014; Robertson et al. 2017; Robertson et al. 2020).

High-fidelity models, such as Computational Fluid Dynamics (CFD), are reserved for the final design stages where detailed stress and load predictions are necessary. There are both open-source and commercial software packages available and shown in Table 2.2.

Table 2.2. High-fidelity software for modelling FOWTs (Source: Otter et al. 2022)

Software	**Computational method**
OpenFOAM	CFD
Ansys	CFD + FEM
Star CCM+	CFD
Abaqus	FEM + CFD
Autodesk	FEM

Since the physical basis of FOWT systems is multi-various and interactive, reliable behavior estimation of the system requires the use of Computer-aided Engineering (CAE) techniques. One well-known example is the fully-coupled aero-hydro-servo-elastic FAST model (J. M. Jonkman et al. 2005).

2.1. Simulation Methods for FOWT Platforms

The Boundary Element Methods (BEM), also known as Panel Methods, are commonly preferred numerical methods for solving FOWT systems' platforms. This technique involves discretizing the geometry of the body into surface elements, which are then used to distribute sources, vortices, or doublets of varying intensities. This outcome in an algebraic system of equations that can be used to calculate the velocity potential. Eventually, the integrated pressure over the surface, as determined by Bernoulli's equation, is utilized to calculate the forces acting on the object (Cruz et al. 2016).

For High-Fidelity solutions, many researchers and engineers use Computational Fluid Dynamics (CFD)-based numerical models to simulate platform movements and forces by solving Navier-Stokes Equations. It comes with a significant computational cost. OC6 project investigated free-decay motion tests on DeepCwind semi-submersible

platform to investigate the hydrodynamic damping coefficients and shear effects on the surface where the mesh was refined near platform surface by CFD simulations and validate the mid-fidelity results (Wang et al. 2022) and some of the works done by (Huang et al. 2021; Liu et al. 2017; Tran et al. 2016) coupling floating and turbine effects are examples of CFD studies. If the CFD study is not suitable for the case, potential flow or Morison's equation approaches are alternatives (Cruz et al. 2016).

Viscous-induced excitation or damping is ignored by the potential flow theory, thus Morison's method is inaccurate for large diffracting structures. To understand the fundamental hydrodynamic forces acting on the platform, these constraints must be considered. A popular commercial approach ANSYS™ AQWA® package uses both models simultaneously (Ansys 2013).

When focusing on the High-Fidelity CFD approach for FOWT platforms, it is important to consider the applied studies of Tuned Liquid Column Dampers (TLCD) and Tuned Liquid Multi-Column Dampers (TLMCD). Table 2.3 summarises these studies.

Table 2.3. Summary of related studies.

Authors	**Case**	**Methodology**	**Main Findings**
Zhou et al. 2023	CFD OpenFoam interFoam solver + Prescribed Motion + semi-submersible FOWT	FVM + VOF + No relaxation zone + No mooring lines + internal sloshing only	TLMCD system can significantly reduce the motions.
Zhou et al. 2022	CFD OpenFoam interFoam + No Prescribed Motion + semi-submersible FOWT	FVM + VOF + No relaxation zone applied + Coupled floating-sloshing modelling + mooring lines	TLMCD system can significantly reduce the motions.
Xue et al. 2022	Experimental + CFD OpenFoam interFoam + No Prescribed Motion + semi-submersible FOWT	Model Scaling (Exp.) + FVM + VOF + No relaxation zone + Mooring lines + Coupled floating-sloshing modelling	TLMCD effectively reduces the motion, liquid mass ratio of 2.0% achieving a reduction in maximum pitch motion by 10.84% to 18.53%.

(cont. on next page)

Table 2.3. (cont.)

Authors	Case	Methodology	Main Findings
Coudurier et al. 2018	Analytical Solution	Lagrangian mechanics + internal sloshing only	Comparing different types of TLCDs and found TLMCDs are more effective than TLCDs for motion reduction.

CHAPTER 3

THEORY AND METHODOLOGY

3.1. Hydrodynamics of FOWTs

This section aims to provide a straightforward explanation of the fundamental physics of floating bodies by first investigating the floating mechanism and then looking at the phenomena of wave propagation and the loads from it. Newton's second law, which explains loads from total pressure integration along the body's surface, may be used to explain the dynamics of floating platforms. Marine engineers have struggled to analytically describe the movements of a floating body, even in calm seas, despite the use of linear hydrodynamic theory. High-fidelity methods, such as CFD, are among the techniques that enable accurate calculations.

3.1.1. Description of Ocean Waves

There are various types of waves on the ocean surface shown in Figure 3.1, but the most significant for offshore constructions are wind-driven waves that are influenced by gravity. These waves usually last from 0.1 to 30 seconds (Cruz et al. 2016).

These waves can originate in a remote location with a more regular distribution and longer crests, or they can be produced by the local wind, resulting in irregular and short crests. Ocean waves should be described stochastically as wind-driven wave creation is a dispersive and unpredictable event (Newman 2018). The linear theory also known as The Airy wave theory is often used to describe irregular sea states about a three-hour window by the combination of the elementary monochromatic waves, including both wind-driven and swell waves, through the application of the Fourier transform.

Various energy spectra, denoted as $S(\omega, \theta)$ (Hasselmann et al. 1973), are utilized to describe sea states in relation to the significant wave height H_s (the average of the highest one-third waves) and the average spectrum frequency. Among these, the Joint

North Sea Wave Project (JONSWAP) model (see Figure 3.4) stands out as a widely chosen option for characterizing nearly fully developed seas (Newman 2018).

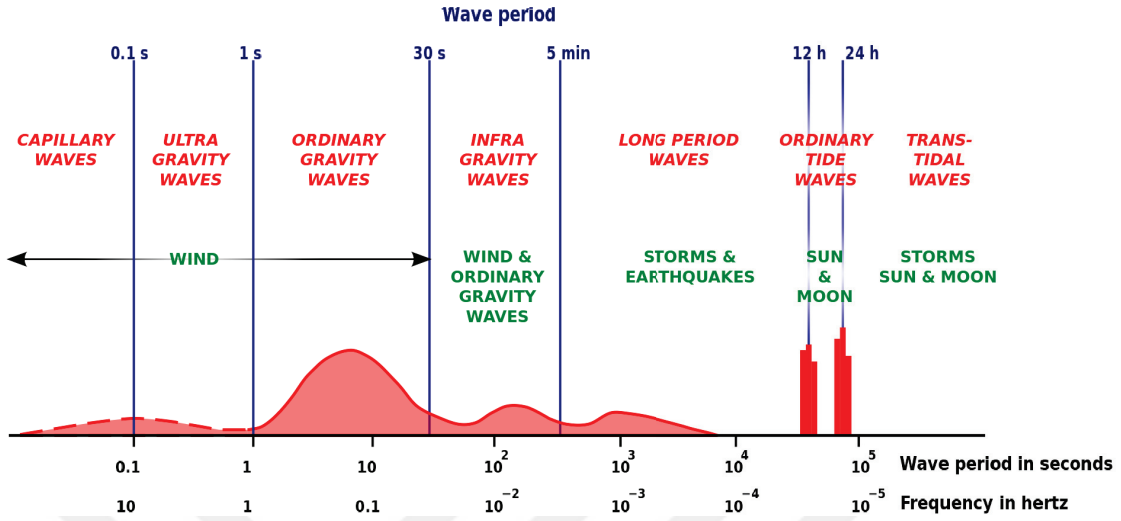

Figure 3.1. Classifying the ocean wave spectrum according to wave period. (Source: Munk 1951)

The standard deviation of the surface, calculated as the square root of the surface variance, is a widely used measure to quantify variations around the mean. It serves as a reasonable metric for assessing fluctuations in surface height. Traditionally, significant wave height, which is defined as four times the standard deviation, has been adopted as a standard measure. $S(f)$ represents the distribution of wave energy across different frequencies. For practical use frequency f used instead of ($\omega = 2\pi f$). The spectrum is associated with a series of characteristic values known as spectral moments, this valuable information about the sea state can be obtained using its moment function for wave number $k = 0, 1, 2, \ldots$ are defined by m_k:

$$m_k(f) = \int_0^\infty f^k S(f)\,\mathrm{d}f \rightarrow H_s \sim 4\sqrt{m_0} \tag{3.1}$$

Here, the spectral moment m_0 represents the surface variance linked to the significant wave height. Large, steep, or non-linear waves, which are typically embedded with a stochastic wave distribution, still require time-domain modeling. Water waves propagate at a different pace than other waves, like sound and light, although each angular wave number has a corresponding frequency and phase speed.

3.1.1.1. Wave Theories

The creation and propagation of gravity waves on the water's surface is an intricate phenomenon, typically modelled using the Navier-Stokes equations in their potential form. To achieve practical and understandable wave descriptions, certain simplifying assumptions must be made. This leads to the development of two primary classifications of wave theories:

3.1.1.2. Linear Waves

Commonly referred to as Airy waves, these waves emerge from the linearization of the kinematic and dynamic boundary conditions at the free surface. In their full expression, these conditions require that the normal velocities of both the fluid and the free surface must be equal at the boundary, and that the fluid pressure must be equivalent to atmospheric pressure. The linear theory simplifies this by neglecting higher-order terms and applying these conditions to the undisturbed free surface plane (Newman 2018). The most straightforward solution to these conditions results in plane progressive waves, where the surface elevation, denoted as η, follows the form:

$$\eta_{(x,t)} = \mathrm{A}\cos(kx - \omega t + \epsilon) \tag{3.2}$$

Here; A represents the wave amplitude, k is the wave number, ω denotes the frequency, λ and L represents wave length and ϵ stands for arbitrary phase. The frequency and wavenumber are connected through the dispersion relation. In deep water, linear waves move in circular orbits with a radius that decreases exponentially with depth when the depth h reaches 0.5λ. Wave drift cannot be captured by linear waves because of its circular motion (Frontera Pericàs 2022).

$$k = \frac{2\pi}{L}; \omega = \frac{2\pi}{T} \tag{3.3}$$

Where k is the wave number, ω denotes the frequency, an impermeable bottom boundary condition must be applied to shallow waters, which results in elliptical trajectories that

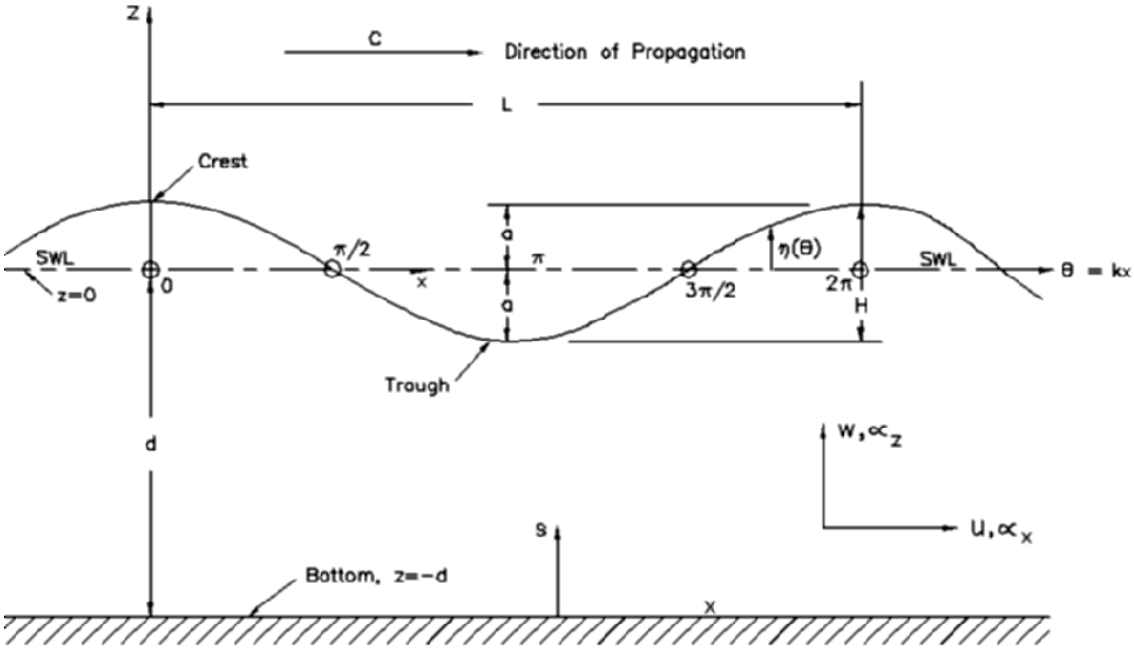

Figure 3.2. Definitions of sinusoidal, progressive wave, elementary wave terms. (Source: Sabatier 2007)

flatten with water depth as shown in Figure 3.3 For these waves, the dispersion relation and wave celerity c are as follows:

$$L = \frac{gT^2}{2\pi} \tanh kh \tag{3.4}$$

$$c = \frac{gT}{2\pi} \tanh kh \tag{3.5}$$

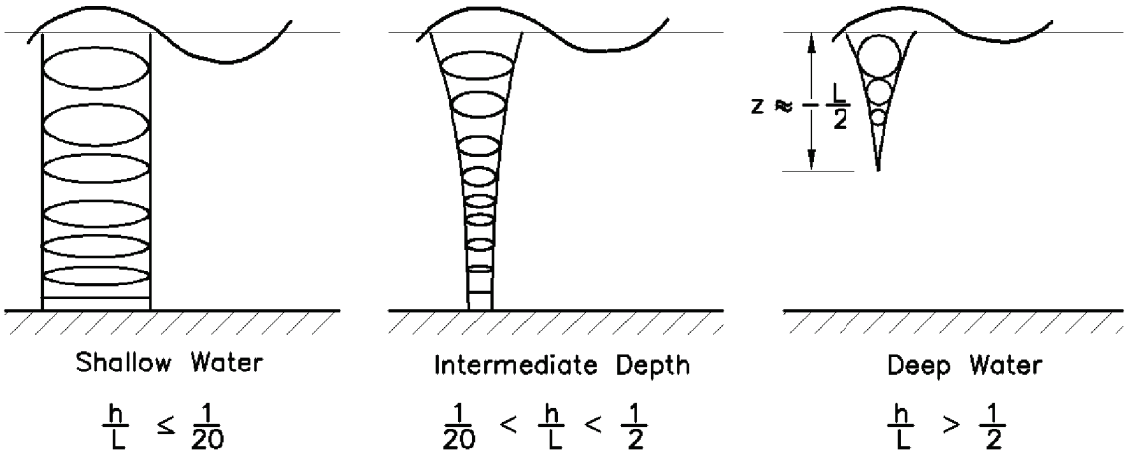

Figure 3.3. Water particle trajectories in different depths (Source: Ippen 1966)

The linear waves has biggest benefit of their ability to superpose, which enables them to replicate arbitrarily irregular wave systems using Fourier series. This process generates a vast number of waves with various frequencies and amplitudes. The spectral density function $S(\omega)$ provides the relationship between these amplitudes and frequencies (Frontera Pericàs 2022).

3.1.1.3. Non-Linear Waves

In the sea and ocean case, waves are non-linear and cannot be considered linear waves (Sarpkaya 2010). Superposition is however possible due to potential flow's linearity. As mentioned before in this section, the Joint North Sea Wave Project (JONSWAP) spectrum model obtained by the Pierson-Moskowitz spectrum which shown in Figure 3.4, is the widely chosen option for non-linear wave definition (Goda 2010).

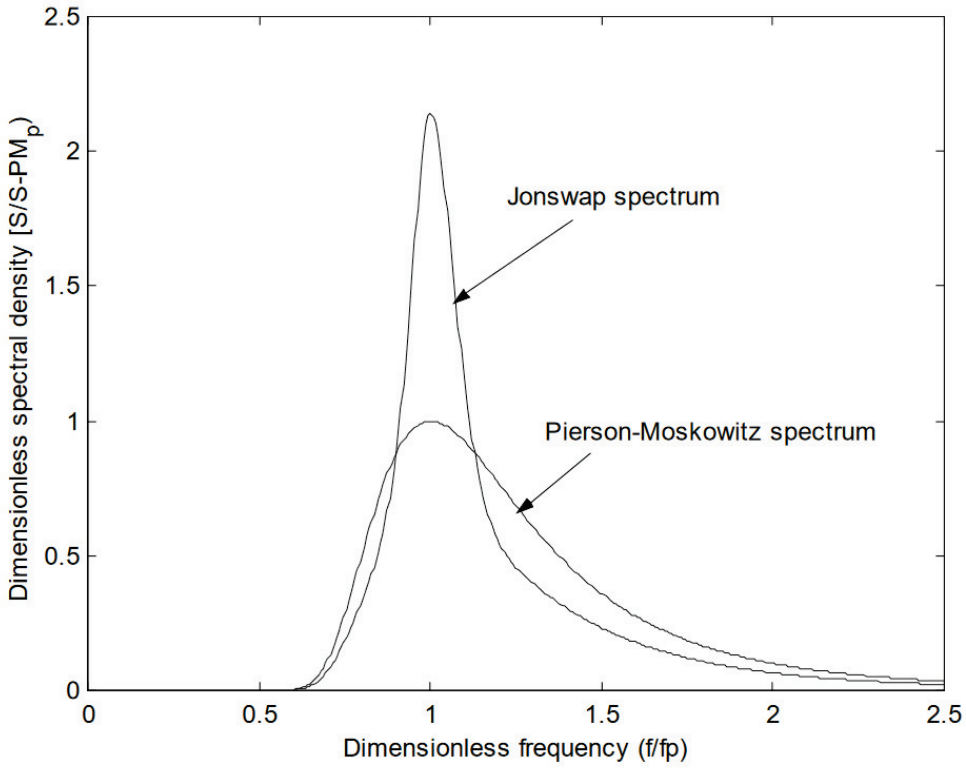

Figure 3.4. The comparison of the Pierson-Moskowitz spectrum and the standard JONSWAP spectrum. (Source: Arntsen. 2000)

Here is the definition of the spectrum $S(f)$ as a function of the spectral peak period

T_p and the significant wave height H_s:

$$S(f) = \beta_{ij} H_s^2 T_p^{-4} \exp\left[-1.25\left(T_p f\right)^{-4}\right] \gamma^{\exp\left[-\frac{(T_p f-1)^2}{2\sigma^2}\right]} \tag{3.6}$$

$$\beta_{ij} \cong \frac{0.0624(1.094 - 0.01915\ln\gamma)}{0.230 + 0.0336\gamma - 0.185(1.9+\gamma)^{-1}} \tag{3.7}$$

$$\gamma = 1 \sim 7, \quad \sigma \cong \begin{cases} 0.07, & \text{if } f \le f_p \\ 0.09, & \text{if } f > f_p \end{cases} \tag{3.8}$$

The γ, peak enhancement factor, is published by (Hasselmann et al. 1973) defined between 1 and 7 with an average of 3.3. The γ defines the sharpness of the spectral peak, it is acceptable to obtain a wave energy spectrum in various shapes. The H_s is the average of the highest 1/3 of wave heights that we can find by the zero-up crossing method.

3.1.2. Hydrostatic Behavior of FOWTs

A moored floating body must be in a vertical equilibrium state when all vertical forces are zero:

$$mg + F_B + N_c T_V = 0 \tag{3.9}$$

$$F_B = \rho_f g \nabla \tag{3.10}$$

Here, m is the structure's mass, F_B is the buoyancy force, N_c is the number of mooring cables utilized for the platform, ρ_f is the fluid density, and T_V is the tension in the cable's vertical component.

By integrating the underwater part of the platform in its undisplaced position, the volumetric displacement ∇ is obtained:

$$\nabla = \int_{-d}^{0} A_{out}(z)\, dz \tag{3.11}$$

Here, d is the draft of the submerged body, and $A_{out}(z)$ is the cross-sectional area of the shell's outer surface at a given depth z.

Assuming that the cut water-plane area A_{wp} remains constant for minor vertical displacements, we may use this information to define the stiffness in the vertical direction k_{33} as follows:

$$k_{33} = \rho g A_{wp} + \Delta T_V \tag{3.12}$$

In the vertical oscillation of the platform, the primary term on the right-hand side is indicative of the resultant unbalanced buoyancy. Meanwhile, the secondary term accounts for the variation in vertical tension (ΔT_V) resulting from the suspension of different lengths of the catenary cable in the mooring lines. Especially, when the mooring system employs a catenary configuration, the unbalanced buoyancy term becomes predominant.

To ensure the static stability of a floating object, vertical equilibrium alone is inadequate. The object must also counteract rotational displacements. The restoring moment in pitch, denoted as M_Y, and in roll, M_X, generated by a rotation θ_2 (in radians), is crucial for maintaining stability.

$$M_Y = [\rho_f g \nabla \overline{GM} + k_{55m}]\theta_2 \tag{3.13}$$

where the metacentric height is denoted by $\overline{GM}$ and the mooring-induced increased pitch stiffness is represented by k_{55m}.

$$\overline{GM} = BM + z_B - z_g \tag{3.14}$$

$$BM = \frac{I_{wp}}{\nabla} \tag{3.15}$$

Here, z_B is the vertical center of buoyancy, z_g is the vertical center of gravity, BM is the distance between the metacenter and buoyancy center, and I_{wp} is the principal second moment of the water-plane area considered for Figure 3.5. The horizontal directions are restoring by moorings:

$$k_{11} = k_x = \frac{\Delta \sum T_H}{\Delta u_1}, \quad k_{22} = k_y = \frac{\Delta \sum T_H}{\Delta u_2} \tag{3.16}$$

The concepts of surge and sway excursions, denoted as u_1 and $u_2$respectively, along

with the linearized restoring stiffness coefficients k_x and k_y, are critical for understanding the dynamics influenced by mooring lines. The tension-excursion relationships that are seen when a displacement, (ΔX or ΔY), is introduced into the system are the source of these stiffness coefficients. By examining the resulting unbalanced horizontal tensions, one can ascertain the respective stiffness values. This methodology is equally applicable to yaw motion analysis. Moreover, the interdependence of surge and pitch can be quantified through the coupled surge-pitch stiffness, providing a comprehensive framework for evaluating the system's dynamic behaviour. And the vertical distance to the fairlead connection is shown by z_f.

$$k_{15} = k_{51} = k_x \cdot z_f \tag{3.17}$$

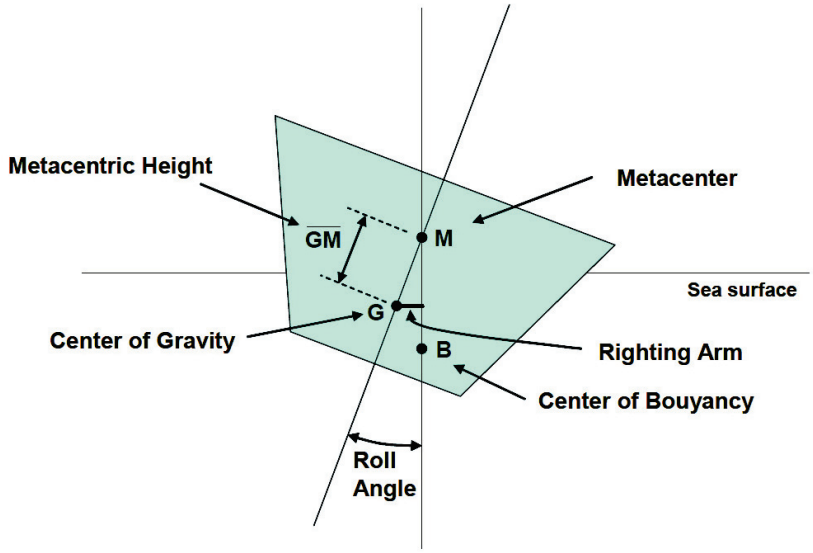

Figure 3.5. Simplified Diagram of Metacenter and Metacentric Height
(Source: Doerry 2008)

3.1.3. Wave-Structure Interaction Loads

Waves and floating bodies interact in a mutual way, where the body submerged in the fluid changes the fluid and the body's existence influences the fluid. Assuming the validity of the linear theory, the resultant loads arising from this reciprocal interaction

can be decomposed into a superposition of more fundamental load sources: Excitation, Radiation and Drag loads.

Excitation loads arise from incident and scattered waves, caused by disturbances in a body. If the unsteady pressure from incident waves isn't influenced by the body's presence, these are called Froude-Krylov loads (Newman 2018).

Radiation loads result from the body's motions, with waves radiating away, extracting energy. These loads, which cause damping and added mass effects, depend on the body's velocity and acceleration and vary with wave frequency.

Drag loads, driven by viscosity and boundary layer detachment, are typically confined to the boundary layer but can cause energy dissipation through vortex shedding when detached. They are highly non-linear, similar to slamming, breaking waves, rogue waves, and ringing (Rainey 2007). Non-linear excitation loads also arise from non-linear waves, such as difference-frequency loads. These are particularly significant for FOWTs due to their high energy content at low frequencies, potentially exciting the first structural modes.

Morison's equation approximates hydrodynamic loads by combining inertial, Froude-Krylov, and drag forces:

$$\mathbf{F} = \rho \mathrm{V} \dot{\mathbf{u}} + \rho c_a \, \mathrm{V}(\dot{\mathbf{u}} - \dot{\mathbf{v}}) + \frac{1}{2} \rho c_d \, \mathrm{S}(\mathbf{u} - \mathbf{v}) \|\mathbf{u} - \mathbf{v}\| \tag{3.18}$$

Here, $\mathbf{u}$ and $\mathbf{v}$ represent wave and body velocities, V is the submerged volume, S is a reference area and c_d and c_a are drag and added mass coefficients, depending on the body's shape and flow regime. This equation, excluding diffraction effects, is best suited for slender bodies.

3.2. Computational Fluid Dynamics (CFD)

Computational Fluid Dynamics (CFD) encompasses numerical techniques used to solve the Euler or Navier-Stokes equations, particularly in their incompressible form:

$$\frac{\partial \mathbf{u}}{\partial t} + \nabla \cdot \left(\mathbf{u}\mathbf{u}^T \right) - \nu \nabla^2 \mathbf{u} = -\frac{1}{\rho} \nabla p + \mathbf{q}, \quad \nabla \cdot \mathbf{u} = 0 \tag{3.19}$$

Here, $\mathbf{q}$ represents a general momentum source term. The most complex aspect of these equations is the non-linear convection term, which is responsible for turbulence. Various methods address this term differently:

Direct Navier-Stokes (DNS): Captures all turbulence scales without assumptions, crucial for research but computationally expensive, scaling with the cube of the Reynolds number (Re), making it impractical for most engineering simulations. Large Eddy Simulations (LES): Resolves large turbulent scales and models smaller ones. While less computationally demanding than DNS, it remains costly and Re-dependent in boundary layers, thus impractical for routine simulations. Reynolds-Averaged Navier-Stokes (RANS): Models all turbulent fluctuations, resolving only the mean flow structures. Though computationally cheaper than DNS and LES, it requires empirical turbulence models like the Shear Stress Transport (SST) model, combining the $k-\omega$ model near walls and the $k-\varepsilon$ model elsewhere.

Hybrid approaches, such as zonal coupling and Detached Eddy Simulations (DES), combine RANS and LES methods. RANS introduces additional unknowns, solved using turbulence models that add new equations.

CFD often employs the Finite Volume Method (FVM) for discretization due to its ease of implementation and conservation properties. The domain is divided into control volumes, integrating conservation laws over each. Various time-marching methods exist, with explicit methods requiring smaller time steps for stability, governed by the Courant-Friedrichs-Lewy (CFL) condition:

$$\mathrm{CFL} = \Delta t \frac{\|\mathbf{u}\|}{\Delta x} \leq 1 \tag{3.20}$$

y^+ is a non-dimensional wall distance metric used to ascertain the location of a control volume within the boundary layer. It is defined by the equation:

$$y^+ = \frac{u_\tau y}{\nu} \tag{3.21}$$

Here, y is the distance from the wall, ν is the kinematic viscosity, $u_\tau = \frac{\tau_w}{\rho}$ is the friction velocity, τ_w is the wall shear stress, and ρ is the fluid density.

When y^+ <5, the cell is situated within the viscous sublayer, characterized by

the relation $u/u_\tau = y^+$. Conversely, for y^+ >30, the flow resides in the log-law region. And, Wall functions are implemented to reduce the number of cells required to model a domain, especially near walls where the viscous sublayer is not fully resolved. Instead of resolving the sublayer completely, the first computational node is placed in the log-law region, typically within the range $30 < y^+ < 100$. This method can encounter challenges in the areas of flow separation and reattachment (Ferziger et al. 2002).

Popular algorithms for solving these systems include SIMPLE for steady-state and PISO for transient simulations. Well-known CFD software include COMSOL, Ansys FLUENT/CFX, STAR-CCM, and as we used in this thesis, OpenFOAM; all include customized pre and post-processing options.

3.2.1. Multiphase Flow and the Volume of Fluid (VOF) Method

These previously mentioned theories are followed in the CFD modelling of floating platforms. By integrating the pressure loads from the CFD solver over the surface, one can determine the total forces and moments on the floating body. Since the 1960s, several techniques have been developed to computationally address multiphase issues (Prosperetti et al. 2009). Define a free surface between water and air necessitates the Volume of Fluid (VOF) formulation.

Introduced by Hirt and Nichols in 1981 (Hirt et al. 1981), the VOF method effectively represents free surfaces in Eulerian simulations. It employs an indicator scalar field $\alpha \in [0, 1]$ for each cell, denoting the volume ratio of a phase—typically, $\alpha = 0$ for gas and $\alpha = 1$ for liquid. The original method used a search algorithm to define the free surface, with boundary cells having non-zero α values and neighbouring zero-valued α cells. For visualization, the free boundary is often defined at $\alpha = 0.5$. Alternative methods to VOF include line segments, marker particles, and level set methods (Schmitt et al. 2020).

Similar to turbulence, multiphase flows are naturally multi-scale, with the free surface producing huge bubbles that fragment into smaller structures. Comparable to an LES filter, the VOF approach averages smaller structures while capturing bubbles bigger than grid sizes. Surface tension, dynamic interfaces, small-scale interactions, turbulence modelling, and phase mixing are examples of multiphase flow difficulties that are outside

this research. Typically, the Navier-Stokes equations are supplemented with a transport equation via the VOF method (Berberović et al. 2009):

$$\frac{\partial \alpha}{\partial t} + \nabla \cdot [\mathbf{u}\alpha] + \nabla \cdot [\mathbf{u}_r(1-\alpha)\alpha] = 0, \quad \phi = \alpha\phi_l + (1-\alpha)\phi_g \tag{3.22}$$

$$\mathbf{u}_r = \min\left(c_\alpha \|\mathbf{u}\|, \max(\|\mathbf{u}\|)\right) \cdot \hat{\mathbf{n}} \tag{3.23}$$

Here, fluid variables ϕ, such as velocity field $\mathbf{u}$, density ρ, or viscosity μ, are computed as weighted averages based on the volume fraction of liquid and gas. Equation 3.22 describes the advection of the indicator field and includes a heuristic surface compression term, $\nabla \cdot [\mathbf{u}r(1-\alpha)\alpha]$, to prevent surface smearing. The vector $\mathbf{u}r$, normal to and directed towards the free surface, acts as a compression term sharpening the free surface. The normal vector $\mathbf{n}$ of the free surface is determined by the direction of the steepest α change, and the coefficient $c_\alpha \in (0, 2)$ regulates the compression effects.

3.2.2. Dynamic Mesh Structures

In CFD simulations, capturing the details near walls, such as boundary layer transitions, separation, and stall, is crucial. To achieve this, the mesh is often refined near the bodies, sometimes including prism layers perpendicular to the surface. When the body moves over time, such as rotating blades or floating structures, dynamic mesh methods are employed to accommodate these changes without regenerating the grid at each time step, which would be inefficient. Several techniques are available to handle moving boundaries (Frontera Pericàs 2022):

The Overset/Chimera Grid combines a static background mesh with an overlapping moving body-conformal mesh. Information is exchanged between zones through interpolation in the overlapping regions, allowing for large displacements and rotations while maintaining boundary layer quality. However, it can be computationally expensive due to the search algorithms needed to identify overlapping cells.

Morphing Mesh involves a single mesh adapting to the moving body's motion. In grid connectivity schemes, nodes move based on their neighbors, while in point-by-point schemes, nodes move independently. These methods suit elastic deformations and

topology changes but can introduce errors with larger displacements.

The Moving Mesh technique aims to move the entire domain. This approach is especially useful for cases involving sloshing tanks. To implement prescribed motion, solid body motion must be assigned to the entire domain.

Adaptive Mesh Refinement (AMR) dynamically refines the mesh in specific regions based on scalar fields or gradients. This method changes the number of grid cells during computation, which does not preserve the initial mesh topology.

The Multiple Reference Frame (MRF) technique divides the computational domain into non-overlapping blocks, each with its own rotation axis and speed. Source terms are added to the equations for non-inertial loads like centripetal and Coriolis forces. This method aims to capture the steady-state solution of an unsteady problem rather than being a true dynamic mesh technique.

The Immersed Boundary (IB) method represents fluid and solid bodies using Eulerian and Lagrangian formulations, respectively. The mesh includes fluid, solid, and boundary elements, and the equations are modified near the boundaries to incorporate boundary conditions. This method handles large deformations and topology changes but can struggle with interpolation and capturing boundary layers accurately.

Sliding Mesh simulations are conducted across disconnected but adjacent mesh domains moving relative to each other, with interface zones ensuring continuity of field values. Cylindrical domains are used for simple cases, while spherical subdomains are used for bodies rotating in multiple degrees of freedom.

Dynamic meshes inherently make simulations unsteady, increasing stability and accuracy requirements compared to static meshes. They can experience instantaneous accelerations and velocities that affect the flow, necessitating robust numerical schemes and solvers. Mesh quality must be monitored, especially for morphing meshes, as large displacements or rotations may degrade quality and numerical stability.

For Floating Offshore Wind Turbines (FOWTs), morphing and overset meshes are most suitable. (Windt et al. 2018; Windt et al. 2020) compared these methods in OpenFOAM for Wave Energy Converters (WEC) and found that both yielded similar results, though overset meshes were more costly. Morphing meshes are recommended for small motions that do not degrade mesh quality, while overset techniques are versatile and robust for large motions across multiple degrees of freedom (Decorte et al. 2019).

3.2.3. Fluid-Structure Interaction (FSI)

Floating turbines are significantly affected by aerodynamic and hydrodynamic forces resulting from interactions between wind and waves with the rotor and platform. The position and motion of the platform, dictated by either elastic or rigid body equations, play a critical role in these forces. This interaction, known as fluid-structure interaction (FSI), applies pressure loads inducing movement in the structure, which then alters the interface between the body and fluid, afterwards changing the flow field and the forces acting on the structure. This creates a closed-loop system between the solid and fluid domains.

Basic iteration methods involve fixed-point modifications of serial and parallel schemes, with under-relaxation needed for stability. Akiten's method, using adaptive under-relaxation, is more stable than traditional Gauss-Seidel. For faster convergence, quasi-Newton methods can be implemented, solving the minimization problem of the interface residual. (Bruinsma et al. 2018) compared two methodologies to tighten FSI coupling in floating body simulations: under-relaxation applied to the body's mass centre acceleration and a predictor-corrector method with sub-iterations for both fluid and rigid body equations.

The predictor-corrector method, applying an under-relaxation factor to the pressure field, was more effective at eliminating oscillations. Similarly, (Dunbar et al. 2015) compared loosely and tightly coupled methods, with the latter using Akiten's dynamic under-relaxation method.

3.2.4. Rigid Body Dynamics

The complex interaction between hydrodynamic and aerodynamic forces and the motion of the platform is a result of the extra degrees of freedom found in Floating Offshore Wind Turbines (FOWTs). Rigid body dynamics play a fundamental role in controlling this interaction. Assuming all acting forces on the FOWT are known, the platform's movement can described by the Newton-Euler equations, which are a set of second-order differential equations (Frontera Pericàs 2022):

$$m\ddot{\mathbf{d}} = \sum \mathbf{F}_i = \mathbf{F}_{\text{hydro}} + \mathbf{F}_{\text{aero}} + \mathbf{F}_{\text{moor}} + \mathbf{F}_{\text{grav}} \tag{3.24}$$

$$\underline{\mathbf{J}}\ddot{\boldsymbol{\phi}} + \dot{\boldsymbol{\phi}} \times (\underline{\mathbf{J}} \cdot \dot{\boldsymbol{\phi}}) = \sum \mathbf{r}_i \times \mathbf{F}_i + \sum \mathbf{M}_i + \mathbf{M}_{\text{gyro}} \tag{3.25}$$

Here, m represents the total mass, $\mathbf{J}$ is the inertia matrix about the center of mass G, and $\mathbf{F}_i$ includes the different force vectors. The gyroscopic moment, which accounts for the turbine's rotation, is treated as an external load:

$$\mathbf{M}_{\text{gyro}} = -\dot{\boldsymbol{\phi}} \times \underline{\mathbf{J}_R} \cdot \boldsymbol{\Omega}_0 \tag{3.26}$$

Where $\boldsymbol{\Omega}_0$ is the rotor's constant angular speed and $\mathbf{J}_R$ is the rotor's inertia matrix. This equation shows that the gyroscopic moment is perpendicular to both the floater and turbine axes, influencing yaw during pitch motion.

When the forces $\mathbf{F}_i$ are not explicitly dependent on the state vector, numerical integration is necessary. However, equation 3.26 reveals that gyroscopic loads are proportional to $\dot{\boldsymbol{\phi}}$. Hydrodynamic loads, assuming linear behaviour, can be expressed using linear potential theory, which simplifies interactions to small motions around equilibrium. This leads to the system of equations:

$$(\underline{\mathbf{M}} + \underline{\mathbf{A}})\ddot{\mathbf{x}} + \left(\underline{\mathbf{B}}_{\text{hyd}} + \underline{\mathbf{G}}\right)\dot{\mathbf{x}} + \left(\underline{\mathbf{C}}_{\text{hyd}} + \underline{\mathbf{C}}_{\text{moor}}\right)\mathbf{x} = \mathbf{F} \tag{3.27}$$

Where $\mathbf{x} = [\mathbf{d}, \boldsymbol{\phi}]^T$ is the state vector, $\underline{\mathbf{M}}$ is the mass-inertia matrix, $\underline{\mathbf{G}}$ the gyroscopic matrix, and $\underline{\mathbf{C}}$ the mooring line stiffness matrix. The matrices $\underline{\mathbf{A}}$, $\underline{\mathrm{B}}_{\text{hyd}}$ and $\underline{\mathbf{C}}_{\text{hyd}}$ represent the hydrodynamic added mass, damping, and stiffness, respectively, which are typically obtained using panel methods. The force vector $\mathbf{F}$ includes wave, current, aerodynamic, and gravitational forces, and is usually not expressible in a simple analytical form. This system can be analyzed in the frequency domain to study the natural frequencies and response to waves:

$$\left| \left(\underline{\mathbf{M}} + \underline{\mathbf{A}}^{-1} \cdot \left(\underline{\mathbf{C}}_{\text{hyd}} + \underline{\mathbf{C}}_{\text{moor}}\right) - \lambda \underline{\mathbf{I}}\right| = 0 \right. \tag{3.28}$$

The eigenvalues correspond to the system's natural frequencies. Simplified forms of these frequencies, ignoring coupling, are:

$$\omega^i = \sqrt{\frac{C^{ii}_{\text{hyd}} + C^{ii}_{\text{moor}}}{M^{ii} + A^{ii}_{(w_i)}}} \tag{3.29}$$

Response Amplitude Operators (RAOs) describe the system's response to wave excitation, based on linear hydrodynamics. RAOs are derived from the transfer function:

$$\text{RAO}(\omega) = \frac{|x_i|}{A} = \frac{\mathbf{F}_0}{\underline{\mathbf{C}} - (\underline{\mathbf{M}} + \underline{\mathbf{A}}(\omega))\omega^2 + i\underline{\mathbf{B}}(\omega)\omega} \tag{3.30}$$

In non-linear cases, effective RAOs measure the difference in response with and without wave excitation, tailored to each specific load case (J. Jonkman et al. 2010).

3.3. OpenFOAM Environment and the Finite Volume Method (FVM)

OpenFOAM, an abbreviation for Open Source Field Operation and Manipulation, is a flexible C++ library designed for numerically solving partial differential equations (PDEs) and multi-physics simulations. It is often used to calculate fluid equations in CFD (computational fluid dynamics) by utilizing the finite volume technique (FVM). The PIMPLE algorithm, which is essential to solving coupled multiphase flow and rigid body equations throughout this thesis, will be thoroughly examined and its basic concepts will be clarified in this section.

For a complete overview of the OpenFOAM environment, new users should consult additional resources. (*The official user tutorials and programmer's guides* 2024) offer thorough instructions on case setup, available functionalities, applications, discretization methods, and programming environment. In addition, Tobias Holzmann's book (Holzmann 2019) concentrates on the underlying mathematics and numerical techniques. For practical learning, the OpenFOAM tutorial collection (*Tutorial Guide* 2024) is highly recommended, offering a curated list of tutorials suitable for various experience levels. Similarly, the forum pages (*OpenFOAM – CFD Online Discussion Forums* 2024) are very useful for solving problems that appear during simulations.

3.3.1. Discretization of the Governing Equations

Among the various techniques available for solving the Navier-Stokes equations, the FVM stands out in commercial codes for its conservative nature and robust implementation. This method discretises the simulation domain into a series of control volumes (grid cells), where physical laws are enforced. Within each volume, the integral form of Equation 3.22, derived using Gauss' theorem, is approximated (Moukalled et al. 2016):

$$\frac{\partial}{\partial t}\int_V \rho\mathbf{u}\mathrm{d}V + \int_S \rho\mathbf{u}\mathbf{u}\cdot\hat{\mathbf{n}}\mathrm{d}S = -\int_S p\ \mathrm{d}S + \int_S \underline{\tau}\cdot\mathbf{n}\mathrm{d}S + \int_V \rho\mathbf{q}\mathrm{d}V \tag{3.31}$$

where the shear rate tensor is denoted by $\underline{\tau}$. Typically, fluxes on the cell surface S are estimated using several quadrature methods from the cell average solution. Interpolation approaches couple the governing equations of distinct cells by extracting cell surface values from center values. These equations discretize to produce a matrix system. Once discretized, the FVM assembled distinct matrices for every variable and solved them in discrete, frequently iterative steps.

The time-derivative component of Equation 3.31 needs to be modelled as well for unsteady conditions. Using a general conservation law that represents the semi-discrete form of Equation 3.31, in which the important quantity is denoted by φ:

$$\frac{\mathrm{d}\varphi(t)}{\mathrm{d}t} = f(t,\varphi(t)) \rightarrow \varphi^{n+1} = \varphi^n + \int_{t_n}^{t_{n+1}} f(t,\varphi(t))\mathrm{d}t \tag{3.32}$$

Various implicit and explicit time-marching methods exist to approximate the integral term of this equation.

3.3.2. The PIMPLE Algorithm

Among the numerous sequential (or segregated) solvers in OpenFOAM, this thesis primarily employs the PIMPLE algorithm—a hybrid of the PISO and SIMPLE algorithms—well-suited for fluid-structure interaction (FSI) problems due to its iterative approach. Given the PIMPLE algorithm's critical role in this work, its implementation in OpenFOAM (Greenshields et al. 2022) is described as follows.

3.3.2.1. Pressure-velocity coupling

The FVM solves each variable's unique matrix equation in consecutive solvers. For instance, there are three linear matrix equations for each velocity component in Equation 3.31:

$$\underline{\mathbf{A}}\mathbf{u} = \mathbf{b}, \quad \mathbf{b} = \mathbf{H}(\mathbf{u}) - \nabla p \tag{3.33}$$

The linear terms in this case are included in $\underline{A}$, and the function $\mathbf{H}(\mathbf{u})$ is derived from $\mathbf{u}$ and other sources. Source, non-linear, and pressure terms are contained in the source vector $\mathbf{b}$. The modified mass conservation rule is used to update the pressure after the velocity field has been solved for:

$$\nabla \cdot \mathbf{u} = 0 \rightarrow \nabla^2 p + \nabla \cdot [\nabla \cdot (\mathbf{uu})] = 0 \rightarrow \nabla \cdot \frac{1}{\underline{\mathbf{A}}} \nabla p = \nabla \cdot \left[\frac{\mathbf{H}(\mathbf{u})}{\underline{\mathbf{A}}} \right] \tag{3.34}$$

The system of solving variables proceeds through a method known as "successive substitution," whereby each resolved variable is substituted back into the subsequent equations' source vectors. This predictor-corrector method is encapsulated in three primary steps:

Momentum Predictor; Solve Equation 3.33 for velocity $\mathbf{u}$, explicitly computing the source vector $\mathbf{b}$ based on current velocity and pressure. Pressure Equation; Utilize the newly obtained $\mathbf{u}$ to solve for pressure via Equation 3.34. Momentum Corrector; Update the velocity field by resolving Equation 3.33 with the refreshed velocity and pressure values.

Often, an intermediate flux corrector step follows, interpolating $\mathbf{u}$ to the cell faces. When this sequence is executed once per time-step, it forms the SIMPLE (Semi-Implicit Method for Pressure-Linked Equations) algorithm, suitable for steady-state simulations. For transient simulations, multiple PISO (Pressure Implicit with Splitting of Operators) loops are conducted between the second and third steps, incorporating the flux corrector at the end. The PISO method addresses non-orthogonality by solving the pressure equation several times.

The PIMPLE algorithm integrates the PISO method with an additional overarching

loop, maintaining temporal accuracy for CFL > 1 and facilitating FSI (Fluid-Structure Interaction) coupling (Greenshields et al. 2022). The PIMPLE loop can be fixed or iterated until convergence. To accurately represent TLMCD loads and rigid body motion, a hybrid approach that uses a set number of sub-iterations guarantees a strong coupling of multiphase fluid and rigid body equations. Based on the present rigid body motion, the algorithm uses explicit source term steps for TLMCD loads, integrating these in later iterations. Figure 3.7 shows simplified PIMPLE algorithm diagram.

3.4. Numerical Wave Tank Implementation with The waves2foam Library and Relaxation Zone Method

The waves2foam library, an open-source toolbox developed in 2011 by Jacobsen at the Technical University of Denmark (Jacobsen et al. 2012), facilitates the generation and absorption of free-surface waves using the VOF (Volume of Fluid) method.

The core functionality of waves2foam revolves around explicit relaxation zones, also known as active sponge layers, for wave generation and damping. Within these zones, the solution is a weighted combination of the computed values (e.g., **U** and α) and a target solution. This is expressed as:

$$\phi = (1 - \alpha_R)\, \phi_{\text{target}} + \alpha_R \phi_{\text{computed}} \tag{3.35}$$

The relaxation weight, denoted as α_R, ranges between 0 and 1, while χ_R is a function dependent on the local coordinate within the relaxation zone, also spanning from 0 to 1. This function can be formulated in various ways, including exponential and polynomial forms, and may even be adjusted based on the local CFL number (Jacobsen 2017). Typically, two distinct relaxation zones are established: one at the wave inlet, where the target field is defined by a specific wave theory, and another at the wave outlet, designed to produce an undisturbed wave profile. The latter is crucial for eliminating unwanted wave reflections that might disrupt the simulation, as illustrated in Figure 3.6.

The user may customize the relaxation zones with waves2foam by selecting from a variety of shapes and weights. The study (Jacobsen 2017) shows: that two shapes of relaxation zones are implemented: rectangular and circular, allowing for flexibility

in wave modelling and absorption methods. Rectangular shapes are good for creating physical experiments and circular shapes suitable for simulations of open-sea conditions.

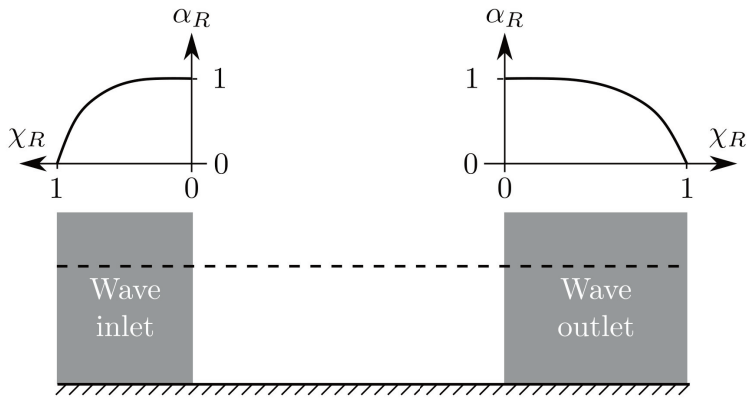

Figure 3.6. A visualization of how $\alpha_R(\chi_R)$ varies for the relaxation zones at the inlet and outlet. (Source: Jacobsen et al. 2012)

The waves2foam library comes with waveFoam solver. The waveFoam solver and waves2foam integrate to enable the study of wave propagation and interactions. It creates waveDyMFoam when mixed with interDyMFoam (with newer OpenFOAM versions named interFoam and incompressibleVOF), which manages moving meshes and captures the free surface. The library has been validated for various applications, including coastal bridge wave loads, beach wave breaking, and modelling floating wave energy converters (Jacobsen 2017).

Additionally, the library also includes utilities such as surface elevation sampling designed for free-surface flows.Wave gauges that track the numerical surface elevation ζ about the starting mean sea level d at the designated locations can be defined by the user. The water percentage α is then numerically integrated along the vertical line $z_0 - z_1$ to get the surface elevation:

$$\zeta = \int_{z_0}^{z_1} \alpha dz - d \tag{3.36}$$

Mooring lines are essential for restraining systems like TLPs (Tension Leg Platforms) against environmental loads, providing stability and preventing fatigue or yield. The waves2foam library features a quasi-steady mooring restraint model, which assumes static equilibrium at each time step and neglects dynamic effects like inertia. This model uses Hooke's law applied to a catenary shape for lines suspended in fluid. Different

formulations are used for the line's freely hanging and seabed-resting portions, allowing for the calculation of the line's shape and restoring tension based on anchor and fairlead positions. While this method includes buoyancy, seabed friction, and elastic stretching, it is limited to lines with uniform properties and horizontal seabeds.

Since the thesis writing date, the last well-implemented version for the waves2foam library was ESI Group OpenFOAM-v2206. Therefore, simulations are carried out on version OpenFOAM-v2012 to avoid potential issues.

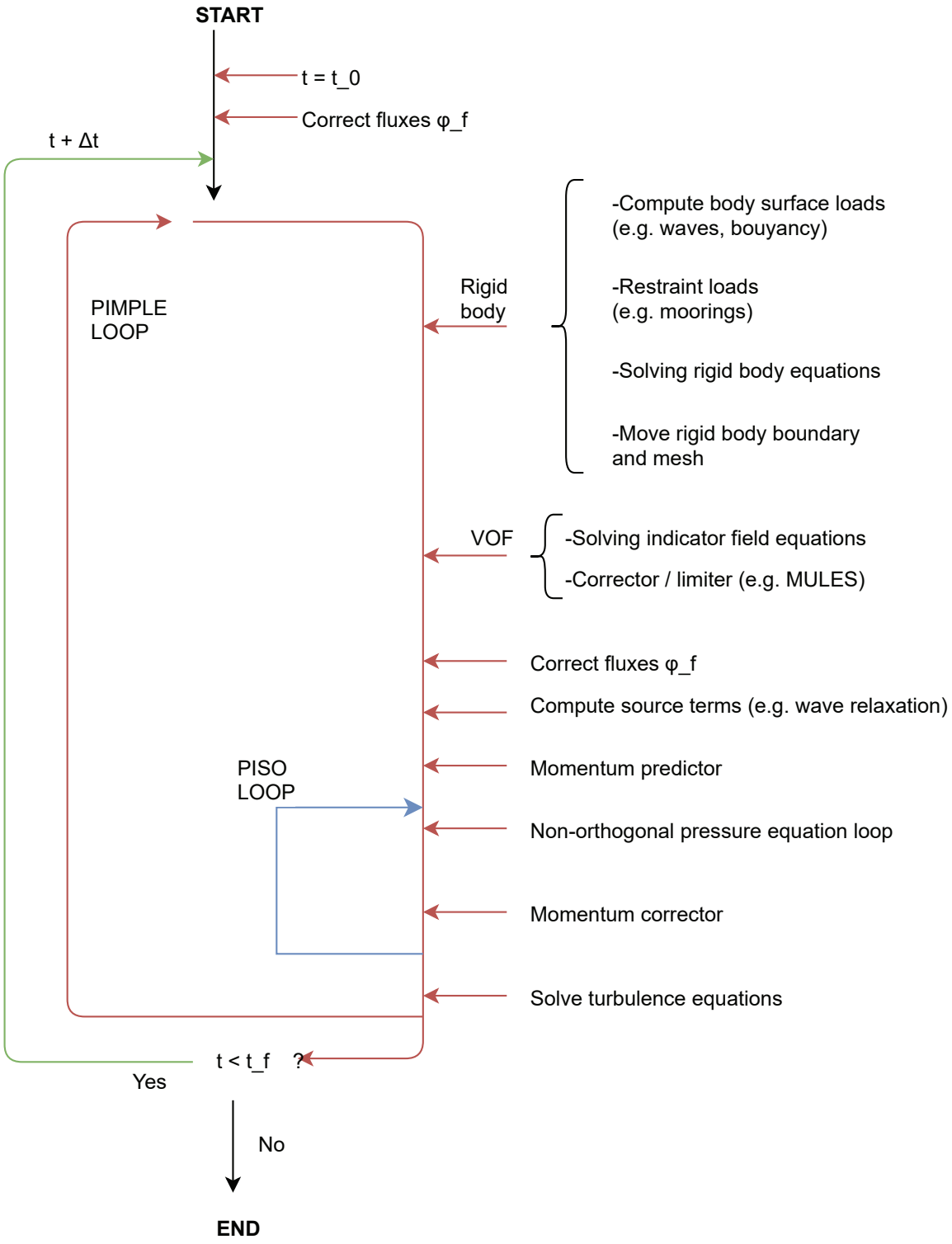

Figure 3.7. Simplified diagram of the PIMPLE algorithm, reproduced by (Greenshields et al. 2022) and (Frontera Pericàs 2022) based on this thesis.

CHAPTER 4

SIMULATIONS

This chapter is meant to evaluate the performance of FOWT by comparing setups using both experimental and CFD studies. In Section 4.1, we will evaluate the ART performance to establish the appropriate setup for internal sloshing calculations, while Section 4.2 will examine a 3D floating cylinder in free decay motion investigation with base-free, moored, and TLCD-applied conditions. And finally Section 4.3 investigates only moored and TLCD-applied 3D floating cylinder performance under regular wave conditions.

All the simulations were performed at TUBITAK ULAKBIM, High Performance and Grid Computing Center (TRUBA HPC resources mounted on CentOS 7.9) by using parallel computing on Intel Xeon 6258R 2.70 GHz 56 Cores on 1 Node and 224 Cores on 4 Nodes.

4.1. Simulations of U-Shaped Anti Roll Tank with Prescribed Motion

Operating limitations, such as maximum acceleration, green water on deck, capsize danger, and passenger comfort, are frequently imposed by the roll motion of ships in a seaway. To reduce uncontrollable rolling motion, roll damping must be improved. There are several ways to lessen roll motion: U-shaped or free-surface ART, active fin stabilizers (which work both forward and at zero speed), and bilge keels. Since the amplitude and phase of the roll-opposing moment are affected by the water flow within the tank, the geometry and internal damping of the tank determine how successful ARTs are at roll-damping. Given the complex and non-linear characteristics of this flow, Computational Fluid Dynamics (CFD) is employed to analyze the intricate flow patterns inside the tank and evaluate its anti-roll performance.

This section examines the sensitivity and validation of the anti-roll performance of passive U-type ART using CFD. Specifically, the study utilizes the incompressible Unsteady Reynolds Averaged Navier-Stokes (URANS) code, incompressibleVOF (for older

OpenFOAM versions interFoam and interDyMFoam). These simulations are done with version OpenFOAM 11 by the OpenFOAM Foundation (Greenshields 2023). This version chosen to implement the latest type of syntax. Comparisons are made between 3D full-scale CFD results validated against model-scale experimental data from (Field et al. 1976) and MARIN experiments conducted by (Gunsing et al. 2014) and CFD studies by (Delaunay 2012), (Thanyamanta et al. 2012), (Kerkvliet et al. 2014) and (Zhou et al. 2023).

4.1.1. Geometry and Grid

The grid structure was created using the blockMesh and snappyHexMesh utilities from a .stl file created by using Blender Open-Source software (Community 2018), following the specifications in Table 4.1 and shown it Figures 4.1a. and 4.1b To improve the accuracy of the wall boundaries, a boundary layer with 10 layers was applied to the ART walls, ensuring that 30 < y^+ <300, as indicated in Figure 4.3. A total of 746,240 hexahedral elements were created as shown in Figure 4.2.

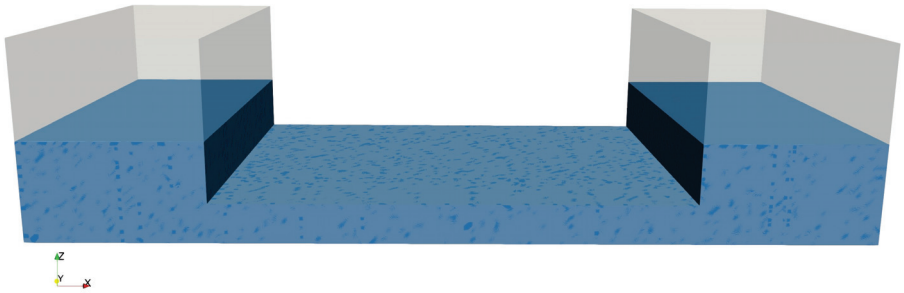

(a) The Present Computational Domain

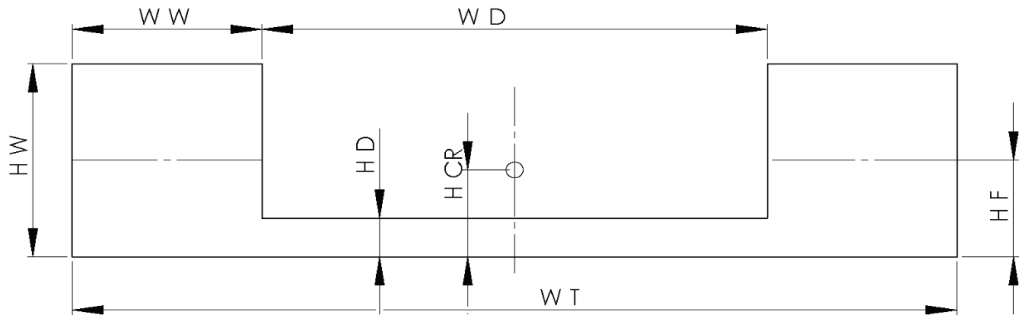

(b) ART Scheme (Kerkvliet et al. 2014)

Figure 4.1. Schematic overview of U-shaped TLCD

Table 4.1. Essential details on full-scale ART and its physical components used in simulations. (Source: Kerkvliet et al. 2014)

Description	**Symbol**	**Magnitude w.r.t. ART bottom**	**Unit**
Total length (x-direction)	W_T	12.800	m
Total width (y-direction)	L_T	5.334	m
Wing tank width	W_W	2.743	m
Wing tank height	H_W	3.048	m
Duct width	W_D	7.315	m
Duct height	H_D	0.610	m
Centre of rotation above bottom	H_{CR}	1.372	m
Water filling height	H_F	1.525	m
Water volume	∇_w	68.43	m^3
Density of water	ρ_w	998	kg/m^3
Viscosity of water	ν_w	1.004×10^{-6}	m^2/s
Density of air	ρ_a	1.118	kg/m^3
Viscosity of air	ν_a	16.315×10^{-6}	m^2/s

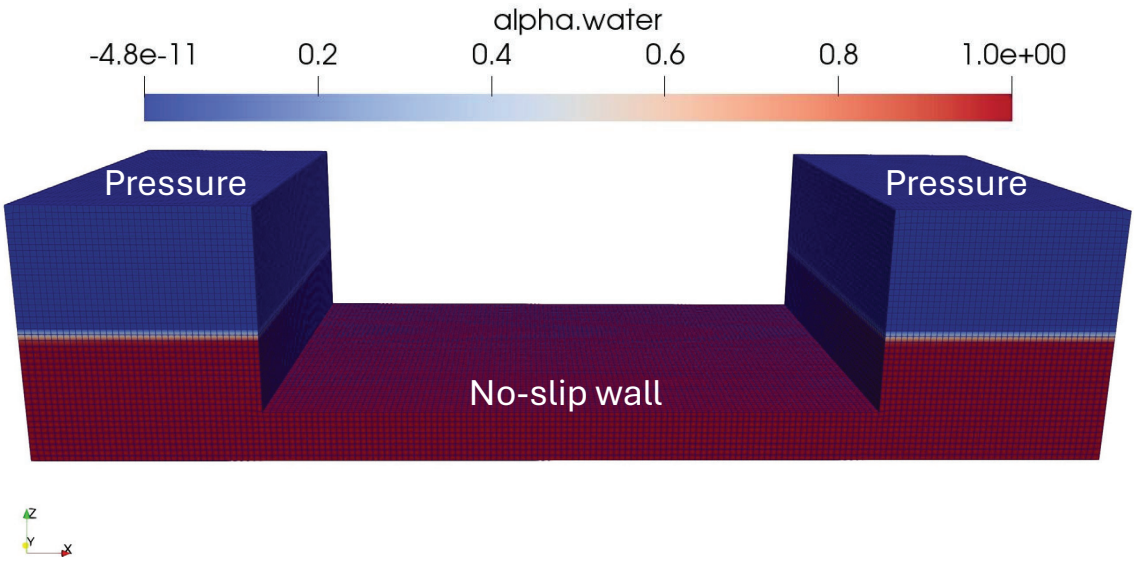

Figure 4.2. ART mesh domain represented with α-water 1 represented red, α-air 0 represented blue, free surface 0.5 represented white with boundary conditions

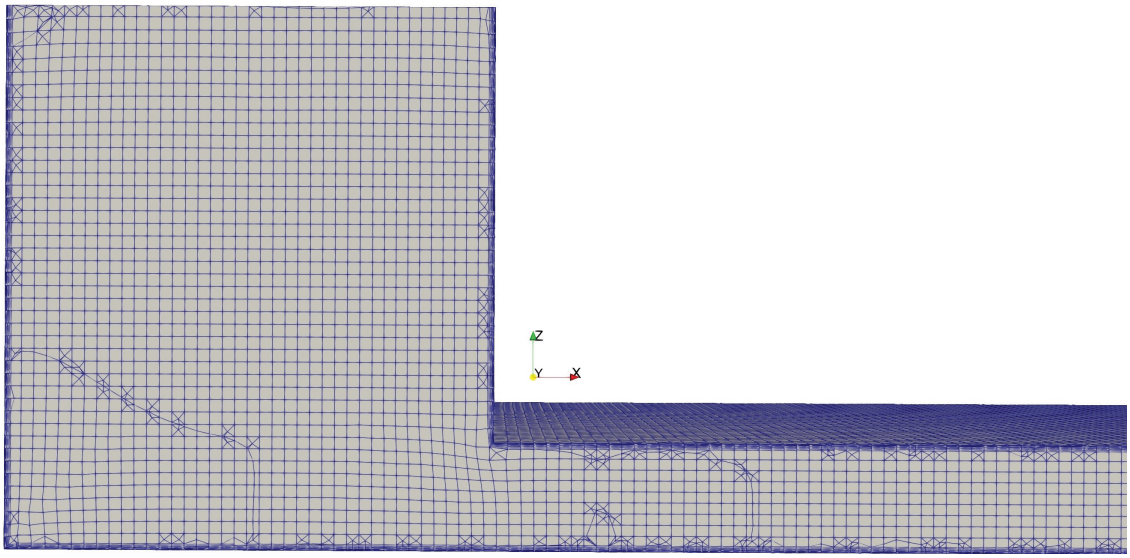

Figure 4.3. ART mesh detail with boundary layer

4.1.2. Initial and Boundary Conditions

The numerical domain measurements have been obtained from works (Kerkvliet et al. 2014) and (Zhou et al. 2023). For simulations, the no-slip boundary condition is applied by movingWallVelocity this condition fixes the velocity to zero at walls for moving bodies, and the atmospherical inletOutlet pressure boundary condition which applies a generic outflow condition and the specified inflow for the case of return flow at two top openings of the columns as shown in Figure 4.2. SST k-ω RANS turbulence model used by (Menter 1994) to capture wall functions properly.

To perform this simulation, the moving mesh approach is applied, it keeps the initial mesh domain the same and moves the whole domain, oscillating-rotating motion applied by oscillatingRotatingMotion in dynamicMeshDict file. ART is prescribed to oscillate at 0.3, 0.5, 0.6, 0.63, 0.65, 0.669, 0.7, 0.8 and 0.9 rad/s, in agreement with other studies with 2° roll amplitude for 12 periods and 100 seconds.

4.1.3. Schemes and simulation controls

The numerical scheme is applied as; time scheme, "Crank-Nicolson 0.7", which shows good agreement with a maximum CFL number of 0.7. The nOuterCorrectors loops are iterate the solution by the same timestep, set to 5 for increased accuracy. For the

free surface capturing by Divergence schemes Gauss interfaceCompression vanLeer 1; applied. For the solver control, on the α water fraction, nAlphaCorr was set 3 iteration and nAlphaSubCycles to 1, Multidimensional Universal Limited for Explicit Solution (MULES) MULESCorr is "yes" with nLimiterIter to 5.

4.1.4. Results and Discussion

All the simulations were performed using parallel computing on Intel Xeon 6258R 2.70 GHz 56 Core on 1 Node and about 10 hours of simulation required for each prescribed natural frequency.

The ART designs are analyzed by calculating the damping coefficient based on the phase lag between water and ship motion. Maximum roll damping should occur at a phase lag of 90 degrees; otherwise, the design will not be optimal and the ART will experience poor motion during operations (Gunsing et al. 2014). Obtained velocity and non-dimensional vorticity graph is represented at Figure 4.4 and 4.6 respectively.

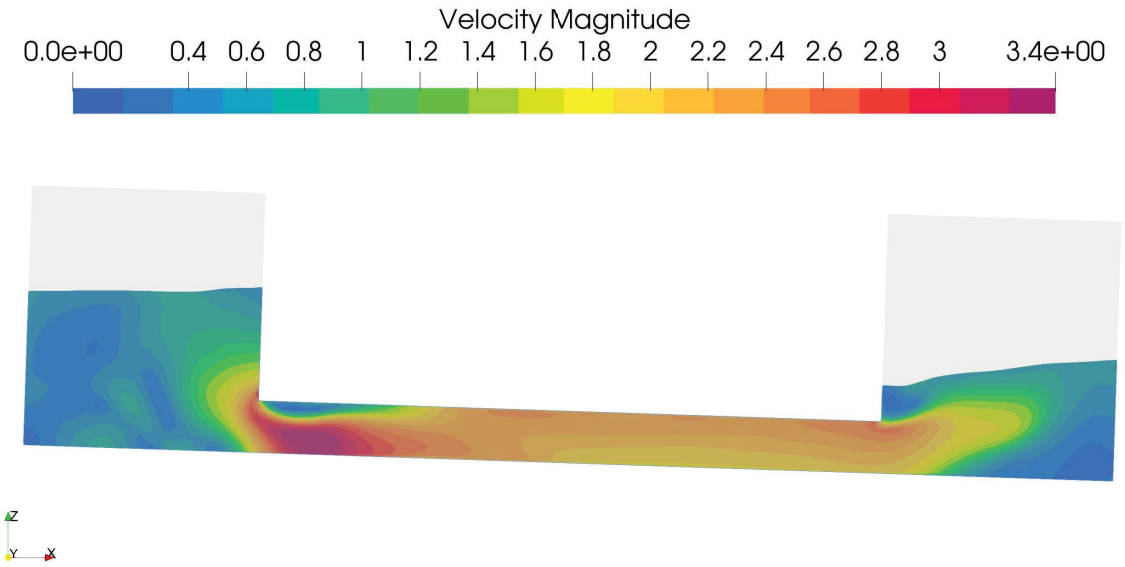

Figure 4.4. Velocity at 9.2nd period.

The results are represented and validated by comparison with (Field et al. 1976) and MARIN experiments (Gunsing et al. 2014) and CFD studies by (Delaunay 2012), (Thanyamanta et al. 2012), (Kerkvliet et al. 2014) and (Zhou et al. 2023) in Figure 4.5.

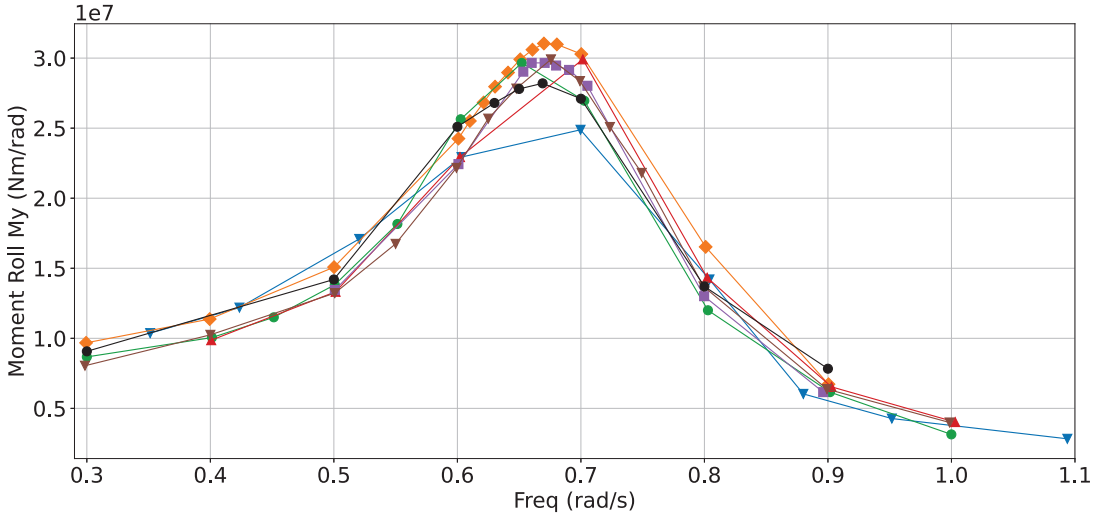

(a) Moment Roll vs Frequency

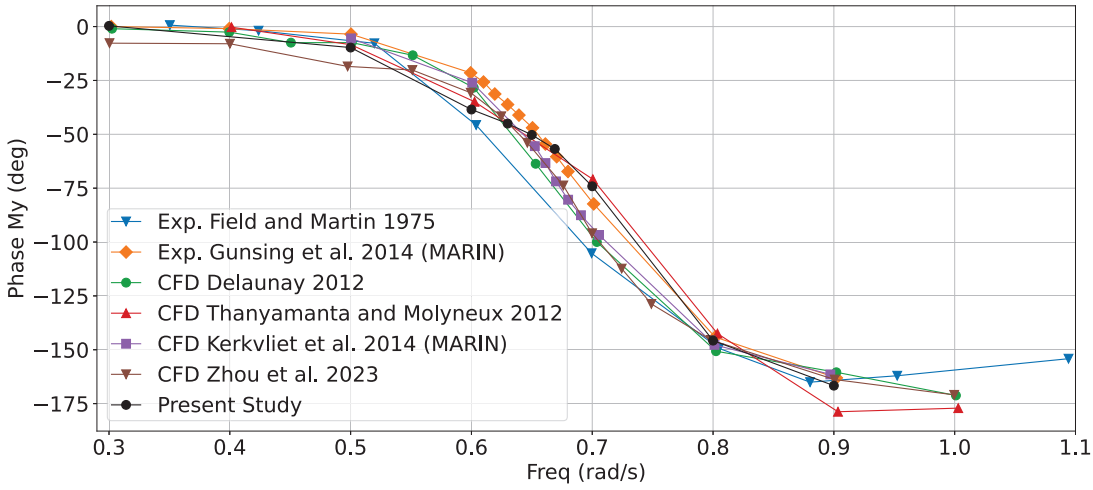

(b) Phase vs Frequency

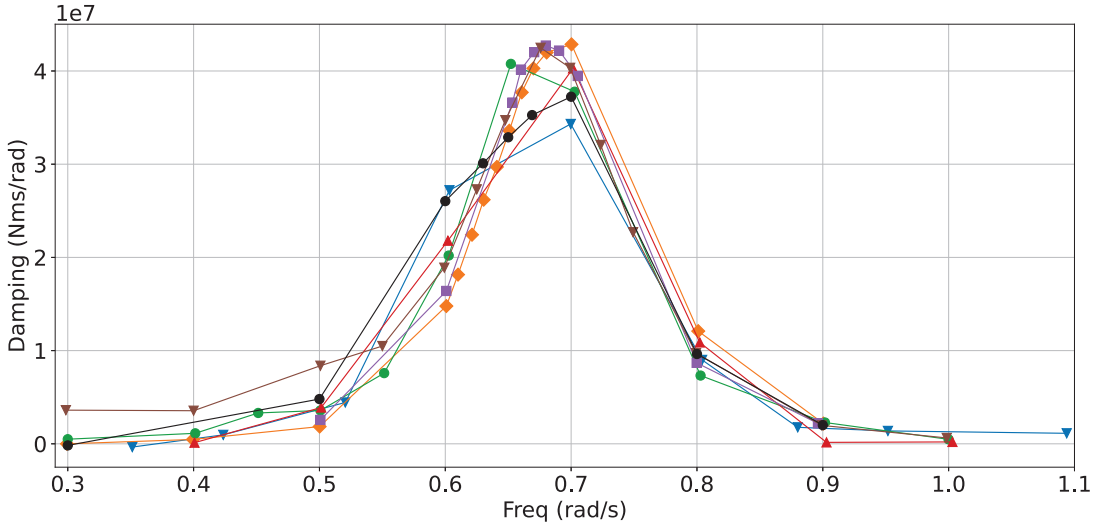

(c) Damping vs Frequency

Figure 4.5. Validation with experimental and CFD data

As discussed before, it's important to consider calculating the damping coefficient for the ART designs to have a good motion state during operations. Here, damping B is calculated by, (Gunsing et al. 2014).

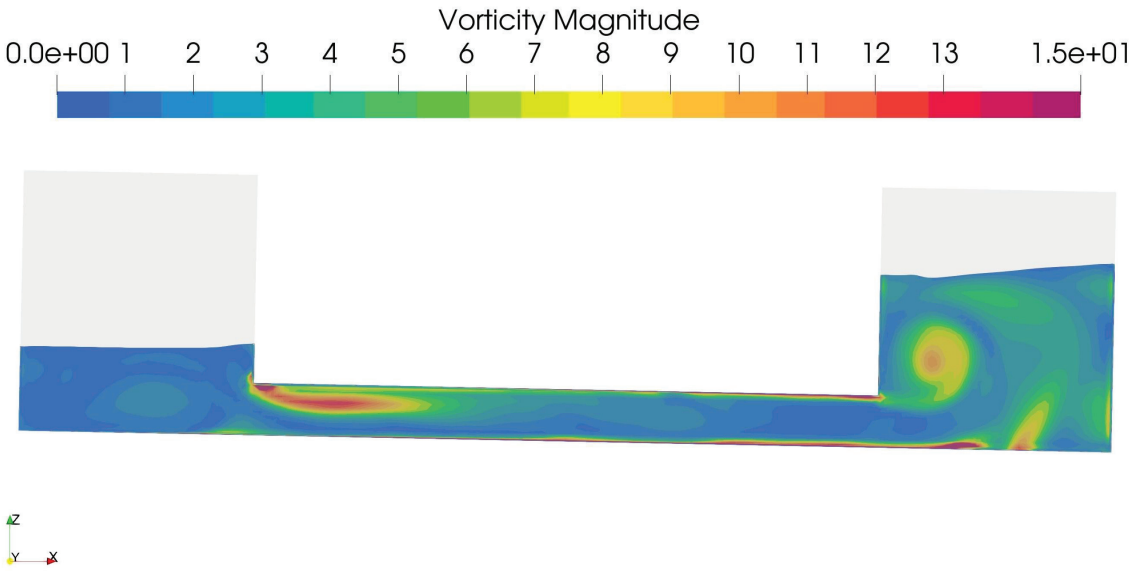

Figure 4.6. Vorticity at 9.4th period.

$$B = -\frac{\mathrm{Im}\left(M_y\right)}{\omega} \tag{4.1}$$

Where M_y is the roll opposing moment which comes from CFD calculation output, imaginary part obtained by using phase lag M_y between water and ship motion. ω is the prescribed natural frequency. With obtaining the roll opposing moment, value is considered the time at which moment values behave steadily on the moment plot. The results of the simulation show good agreement with the reference data within the reasonable uncertainty of the CFD simulations. The maximum roll damping is achieved at 90 degrees of phase lag.

4.2. 3D Cylinder Simulations of Pitch Motion Decay (Free, Mooring and with TLMCD)

Dynamic meshing is one of the important parts of modern CFD, in every application. Several mesh motion methods can be available in OpenFOAM: Morphing and

Overset techniques. The latter, being more suitable for large displacement, will not be followed in the current study. Attention will be paid to morphing-based approaches, more ideal for small displacements. Therefore, this will require setting up the dynamicMeshDict file with appropriate solvers and under particular boundary conditions.

In applying the six degrees of freedom of a rigid body under OpenFOAM, it is imperative to define the following: body properties, initial conditions, constraints, and restraints. All calculations are done concerning principal axes of inertia, about which users are expected to take care when specifying orientations. Discrete computation of strategic external forces, like fluid loads and point forces, occurs at every cell face in the fluid-body interface. OpenFOAM offers two implicit schemes for time integration when solving rigid body equations: Newmark-β and Crank-Nicolson (Greenshields 2023). Both methods offer control over the amount of numerical damping introduced and the implicitness. Sensitivity analysis of the solver and its parameters should be conducted as it has a significant impact on the stability and accuracy of the solution. OpenFOAM implements fluid-structure interaction through a partitioned approach. It is necessary to use many outer-corrector loops in an effort to lower the partitioning error. Reducing the interface residual and tightening the coupling between the solid and fluid domains, the rigid-body equations will be solved once per outer-corrector iteration when the moveMeshOuterCorrectors flag is enabled on the PIMPLE solver control sub-dictionary. This will update the mesh. However, the way to obtain a fully coupled system is still very challenging.

In this study, we want to reproduce the experimental work of (Paredes et al. 2015) on wave energy converters (WECs), whereby the decay motion of a cylindrical floater was examined concerning several kinds of constraints, such as unrestricted motion and catenary moorings. (Palm et al. 2016), (Rivera-Arreba et al. 2018) and (Frontera Pericàs 2022) have quantitatively modelled this scenario using CFD, and the results of their modelling will be utilized to validate the existing implementation. Finally, pitch motion will be the only focus of this study with free, moored and TLCD-applied configurations.

4.2.1. Geometry and Grid

The geometry shown in Figure 4.7 and grid structure in Figure 4.9 and 4.10 was created using the background mesh by blockMesh and the cylinder by snappyHexMesh

utility from a .stl file created by using Blender Open-Source software (Community 2018), following the specifications in Table 4.3 which dimensions and parameters obtained from (Paredes et al. 2015) and (Frontera Pericàs 2022) for benchmark the studies on free and moored configurations and TLCD applied by .stl dimensions. The TLCD model used on the cylinder is scaled down to 3% of the U-shaped ART in the previous section 4.1 to fit inside. ART is located at the same rotation point of the cylinder and the top openings open to the atmosphere. Because the mass with filled water was close to the previous cylinder mass, the moment of inertia I_{xx} and I_{yy} set to the 1.04 kgm^2 and I_{zz} is calculated according to the floater density assumed uniform.

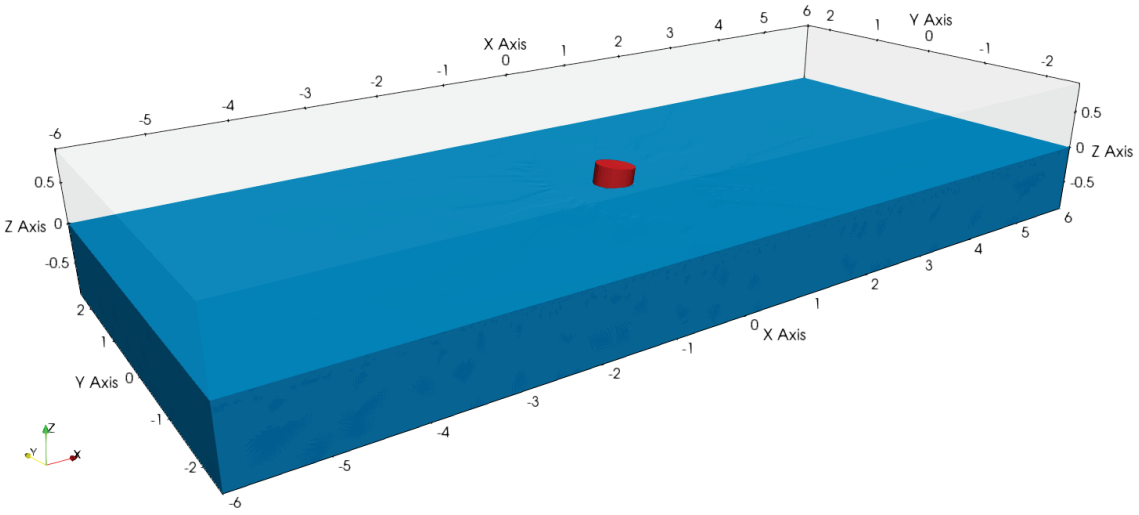

Figure 4.7. The Present Computational domain

The grid resolution is adjusted by using multiple refinement zones to decrease the grid size near the floating body and increase it farther away. There are three refinement levels (n_r) and additional refinement at free-surface is also defined, and the spatial discretization is based on the number of points per cylinder diameter (p.p.c.d.) methodology.

Table 4.2. Masses for different TLCD configurations.

	8%	**4%**
Cylinder mass (kg)	32.82	32.82
Water mass (kg)	2.65	1.34
Total mass (kg)	35.47	34.16

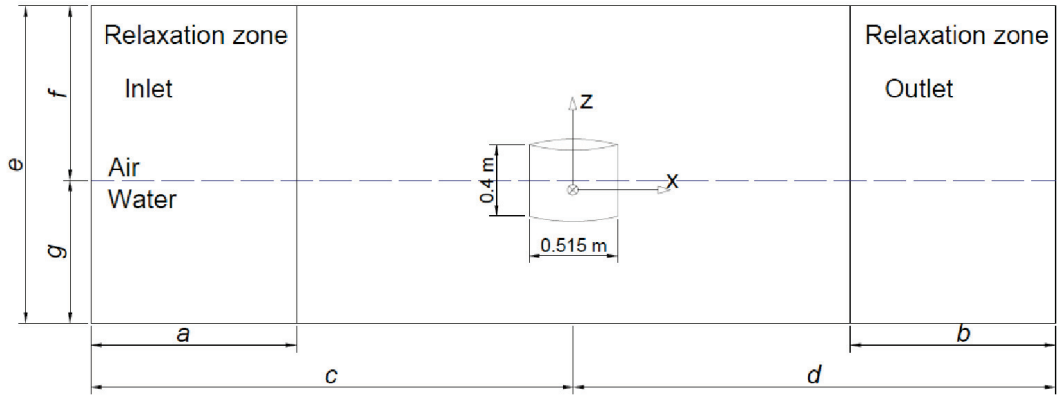

Figure 4.8. Domain Scheme (Source: Rivera-Arreba et al. 2018)

Table 4.3. Numerical domain set-up dimensions and parameters of the floater and mooring line: draft d, mooring line length l_m, height h, inertia moment I_{xx}, center of gravity C_g, and density ρ_m.

Description	**Value**	**Description**	**Value**
m (kg)	35.85	$\mathbf{d_m}$ (m)	0.178
$\mathbf{m_{TLCD}}$ (kg)	35.47	$\mathbf{I_m}$ (m)	6.95
$\mathbf{d_f}$ (m)	0.172	$\boldsymbol{\rho_m}$ $(\mathrm{kg/m^3})$	431.927
$\mathbf{I_{xx}}$ $(\mathrm{kg \cdot m^2})$	0.90	**a** = **b** (m)	3
$\mathbf{I_{xx}}$ (TLCD) $(\mathrm{kg \cdot m^2})$	1.04	**c** = **d** (m)	6 (11.65 D)
h (m)	0.401	**e** (m)	1.8
f = **g** (m)	0.9	**D** (m)	0.515
$\mathbf{C_g}$ (m)	0.0758	Width of the domain (m)	5

This methodology is also used by (Rivera-Arreba et al. 2018) and (Frontera Pericàs 2022). (Rivera-Arreba et al. 2018) found a low difference between 15 and 20, while (Frontera Pericàs 2022) applied 24 p.p.c.d., which also showed good agreement. With all this study's configurations the background mesh size is set to $l_0 = 0.53R$;

$$l_{(n_r)} = \frac{l_0}{2^{n_r}} \tag{4.2}$$

$$\text{p.p.c.d.} = \frac{\text{diameter}}{\text{grid size}} = \frac{2R}{l_{(n_r)}} = \frac{R}{l_0} 2^{(n_r+1)} = \frac{2^4}{0.53} = 30 \tag{4.3}$$

Here, R is the cylinder radius. And the boundary layer defined 5 layers with 100% coverage as shown in Figure 4.10. The final mesh obtained approximately 2.24M hexahedral and polyhedral elements. Due to the large cell count, the renumberMesh utility was used to reduce the matrix system's bandwidth, enhancing linear solver efficiency.

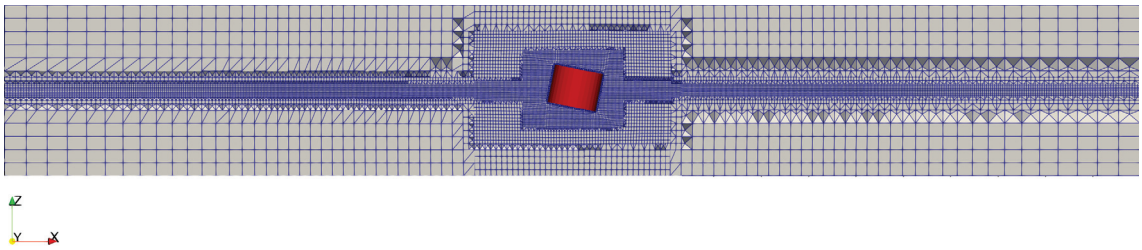

Figure 4.9. Sliced mesh with refinement zones

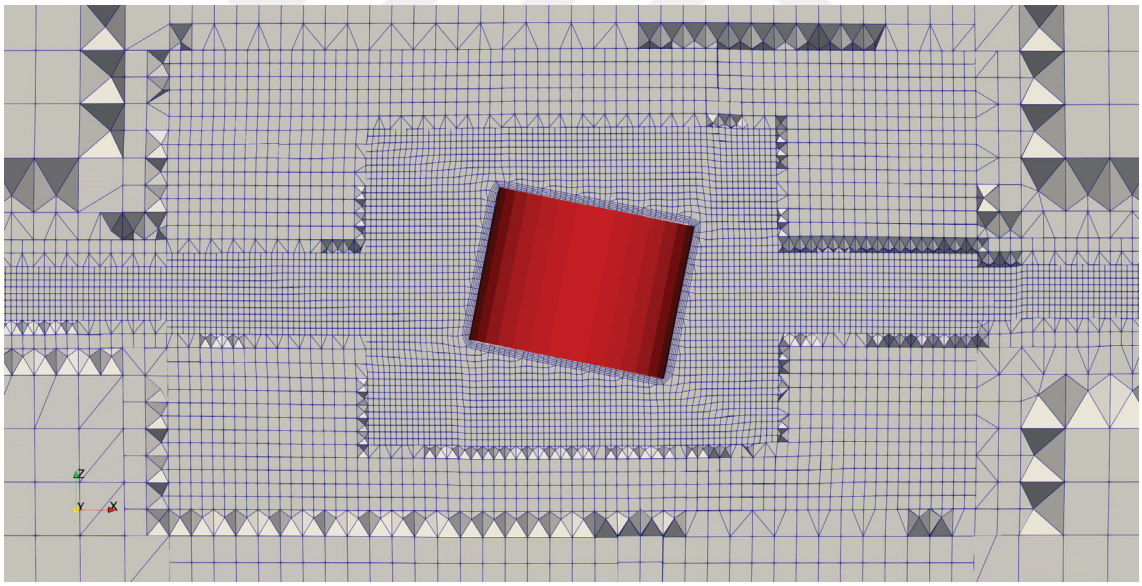

Figure 4.10. Boundary layers around cylinder

4.2.2. Initial and Boundary Conditions

The numerical domain measurements have been obtained from works (Rivera-Arreba et al. 2018) and (Frontera Pericàs 2022). For simulations, the no-slip boundary condition is applied by movingWallVelocity this condition fixes the velocity to zero at

walls for moving bodies, and the atmospherical inletOutlet pressure boundary condition which applies a generic outflow condition and the specified inflow for the case of return flow at the top and slip boundary with the back, front and bottom of the domain. The relaxition zones are defined 3 m same at the inlet and outlet, wave or current didn't applied due to the free-decay motion analysis desired.

To perform this simulation, the morphing mesh approach is applied, with this approach the mesh have been modified by inner and outer distances that control defined at dynamicMeshDict file. No motion constraints were imposed. With attachments at the waterline 0.015 m from the floater, the attachments were defined taking into account the floater's equilibrium position and accounting for initial inclination effects. The quasi-steady catenary mooring restraint model from waves2foam (Jacobsen 2017) was utilized for the moored case. It could handle three mooring line states: simple, resting, and hanging. The three mooring lines were symmetrically placed 120° apart.

Motion amplitude was normalized with initial displacement with $\theta_0 = 8.898°$ for free decay and $\theta_0 = 11.353°$ for moored and TLCD case. TLCD initial water levels are set by setFields file same as free-surface definition where α water fraction is 1 according to TLCD mass ratios are set 8% and 4% of the floater mass as shown in Figure 4.11 to have TLCD's damping effect.

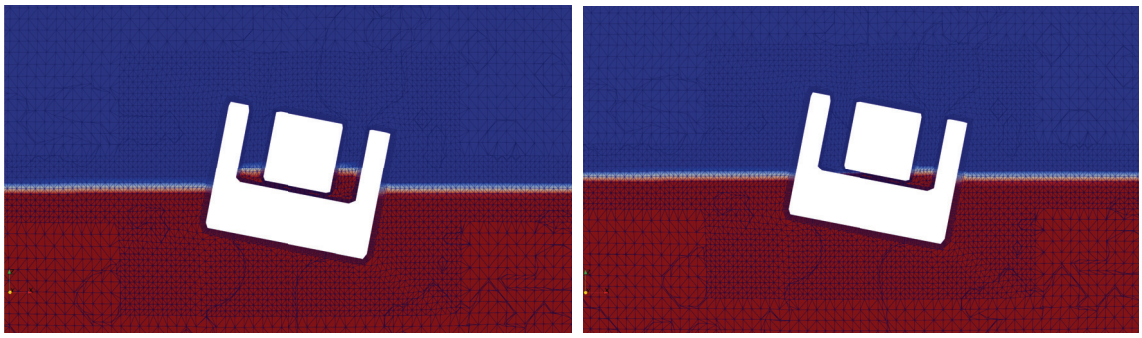

(a) 8% TLCD (b) 4% TLCD

Figure 4.11. Section cut of the computational domain of TLCD applied configuration with initial TLCD water level representations.

Where α-water 1 is represented in red, α-air 0 is represented in blue, and the free surface 0.5 is represented in white.The turbulence model wasn't applied, and implemented as laminar.

4.2.3. Schemes and simulation controls

The numerical scheme is applied as; time scheme, Euler with the maximum CFL number 0.5. For the solver control, on the α water fraction, nAlphaCorr was set 3 iteration and nAlphaSubCycles to 2, Multidimensional Universal Limited for Explicit Solution (MULES) MULESCorr is "yes" with nLimiterIter to 5. The total simulation time aimed for three times the floater's natural period in pitch, $t_f = 3T_\theta = 3.51\,\mathrm{s}$, where T_θ=1.17, comparison with (Rivera-Arreba et al. 2018) and (Frontera Pericàs 2022).

4.2.4. Results and Discussion

The simulations were performed using parallel computing on Intel Xeon 6258R 2.70 GHz 56 Core on 1 Node and about 14 hours for free and moored, 5 hours of each TLCD case simulations required for each configuration.

Motion amplitude was normalized with initial displacement as mentioned in the initial conditions section. To reduce measurement error, experimental testing was conducted at least fifteen times by (Paredes et al. 2015). The oscillation period was calculated as the number of cycles inside the oscillation span divided by the elapsed time between the first and last peak. (Palm et al. 2016) used 7 period, (Frontera Pericàs 2022) used 3 as (Rivera-Arreba et al. 2018). In this study for good comparison, 3 periods were used.

The numerical oscillation periods for all configurations are shown in Table 4.4 and motion types are shown in Figure 4.12 compared with the CFD and experimental studies.

The free-decay test findings, within the anticipated uncertainty of CFD calculations, agree well with the reference data. With Palm's results being the closest to the experimental data, all numerical models underpredict the pitch natural period by a small amount. It is not unexpected that the current simulation and Rivera's study have comparable results given their similar methodologies. Even though the current simulation has a more relative error than the other studies, after normalisation of the motion, we have a more accurate motion state close to the experimental data.

The differences between CFD and experimental results are particularly noticeable in the moored arrangement. This might be caused by small variations in model parameters

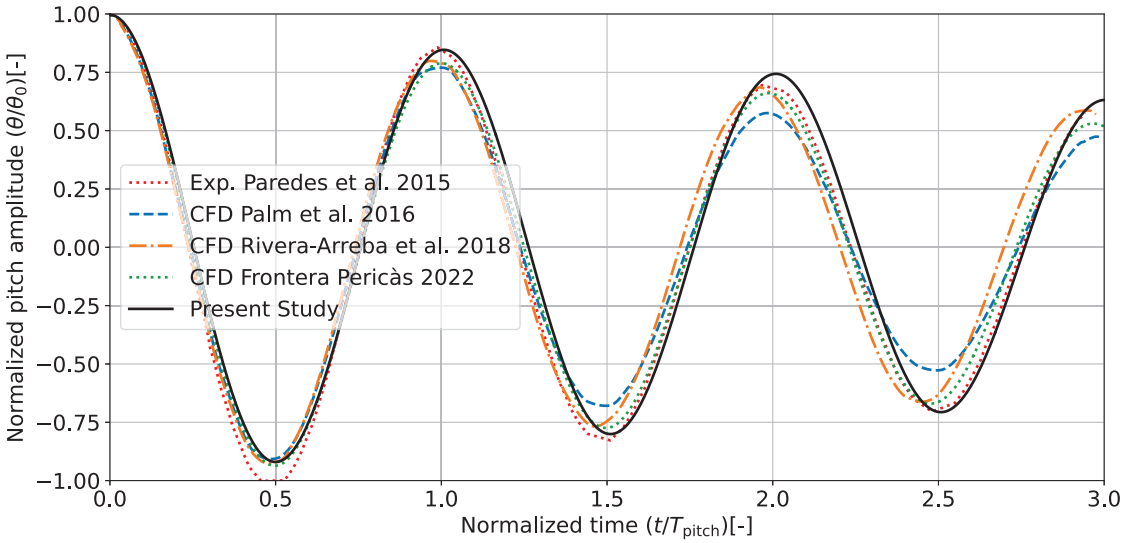

(a) Free Decay Configuration

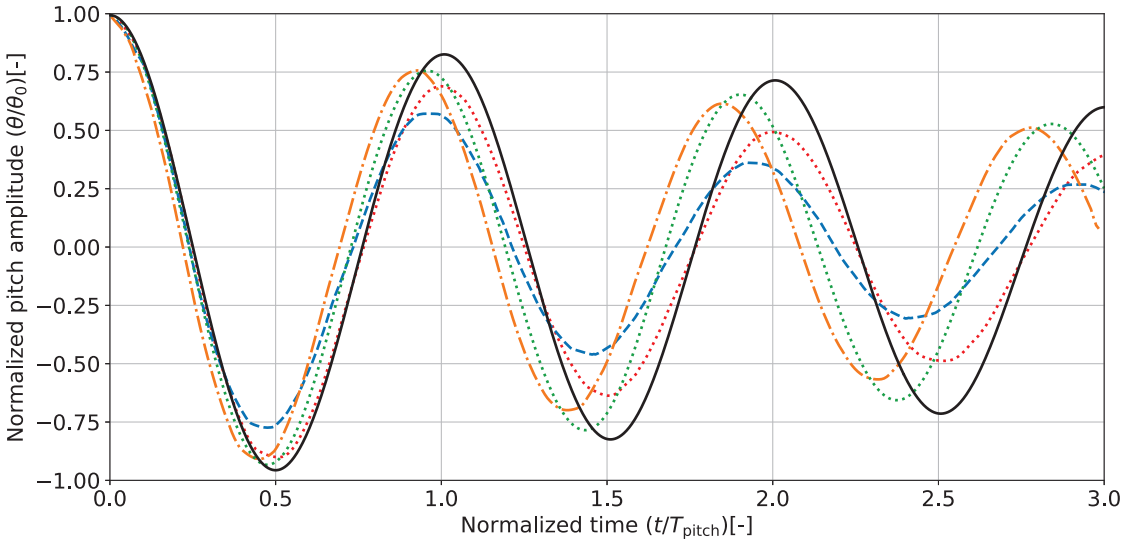

(b) Moored Free Decay Configuration

Figure 4.12. The comparison of the pitch decay motion of the cylindrical floater with experimental and CFD data for both base-free configuration and moored configurations.

and the constraints of the mooring models. In contrast to the free situation, mooring cables introduce stresses in all six DoFs, leading to complex, highly coupled motion.

Table 4.4. Comparison of pitch decay motion periods between experimental and CFD results for free,moored and TLCD applied configurations.

	Oscillation period [s]			**Relative error [%]**	
	Free	**Moored**	**TLCD**	**Free**	**Moored**
Exp. Paredes et al. 2015	1.170	1.163	-	-	-
Palm et al. 2016	1.163	1.136	-	-0.60	-2.32
Rivera-Arreba et al. 2018	1.130	1.050	-	-3.41	-9.72
Frontera Pericàs 2022	1.157	1.110	-	-1.10	-4.55
Present Study	1.117	1.104	1.098	-4.53	-5.07

In Figure 4.13, all simulation motions have been normalized for comparison. The differences in free-decay motion between the base-free configuration and moored configurations are minimal, moored case 6.44% mitigated the motion primarily due to the limitations of the mooring models.

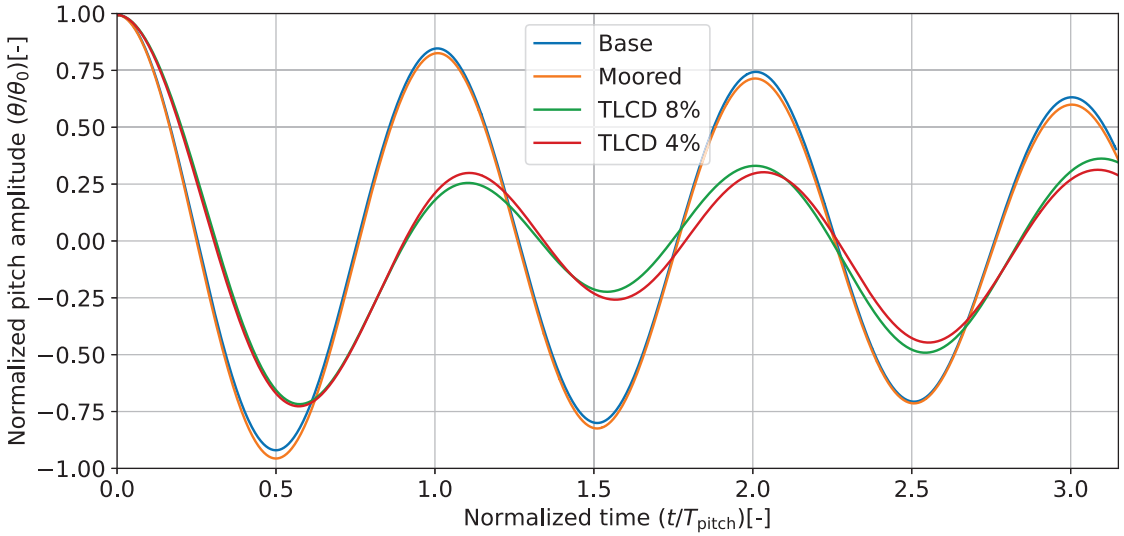

Figure 4.13. The comparison of the pitch decay motion of the cylindrical floater with base-free configuration, moored and TLCD applied configurations.

However, the TLCD configurations significantly reduced the motion amplitude, the 8% maximum was reduced by 40.50% and the 4% maximum was reduced by 47.80%

compared to the moored case. With the amplitude-frequency reduction, simulation time also decreases due to the reduced mesh movement. During the free-decay analysis, the floater with TLCD exhibits a gradual decrease in motion during the initial period, followed by a steady reduction in amplitude after that.

4.3. 3D Cylinder Simulations of the Motion Under Regular Wave Conditions

In this study, we want to implement regular wave conditions into the previous simulation at Section 4.2 of wave energy converters (WECs) with unrestricted motion and catenary moorings. The pitch motion will be the only focus of this study with moored and 4% TLCD-applied configurations. Geometry, grid structure, schemes, and simulation controls are kept the same as in Section 4.2 besides initial displacement was not used.

4.3.1. Initial and Boundary Conditions

The numerical domain measurements remain consistent with those detailed in Section 4.2. During simulations, the no-slip boundary condition is enforced using the movingWallVelocity parameter, which ensures that the velocity is zero at the walls of moving bodies. Additionally, the atmospheric inletOutlet pressure boundary condition is employed, applying a general outflow condition and a specified inflow for return flow scenarios at the top of the domain, while a slip boundary is maintained at the back, front, and bottom of the domain. Relaxation zones are implemented 3 meters at both the inlet and outlet.

Waves are described using the Stream Function Wave Theory developed by Dean (Dean 1965) with the waves2Foam tool (Jacobsen 2017). The wave parameters are defined in Table 4.5.

To perform this simulation, the morphing mesh approach and mooring lines applied as previous simulations. Two configurations are implemented first one is only mooring lines and second one is with mooring lines and 4% TLCD. Initial displacement not applied. The turbulence model wasn't applied, and implemented as laminar. Total simulation time

set 28.8 seconds to see at least 20 oscillation period.

Table 4.5. Regular waves (stream function) parameters.

f[Hz]	T[s]	H[m]	λ[m]	$\frac{d}{gT^2}$	$\frac{H}{gT^2}$
0.83	1.2	0.04	2.23	0.063	0.00283

4.3.2. Results and Discussion

The simulations were performed using parallel computing on Intel Xeon 6258R 2.70 GHz 224 Core on 4 Nodes and about 24 hours for moored, 26 hours for 4% TLCD case simulations required for each configuration.

The implementation of the wave flume is successfully shown in Figure 4.14 by hydrostatic pressure representation. The relaxation zone at the outlet is visible, and the inlet generated wave can be seen by higher pressure values at the wave crest and lower values at the trough.

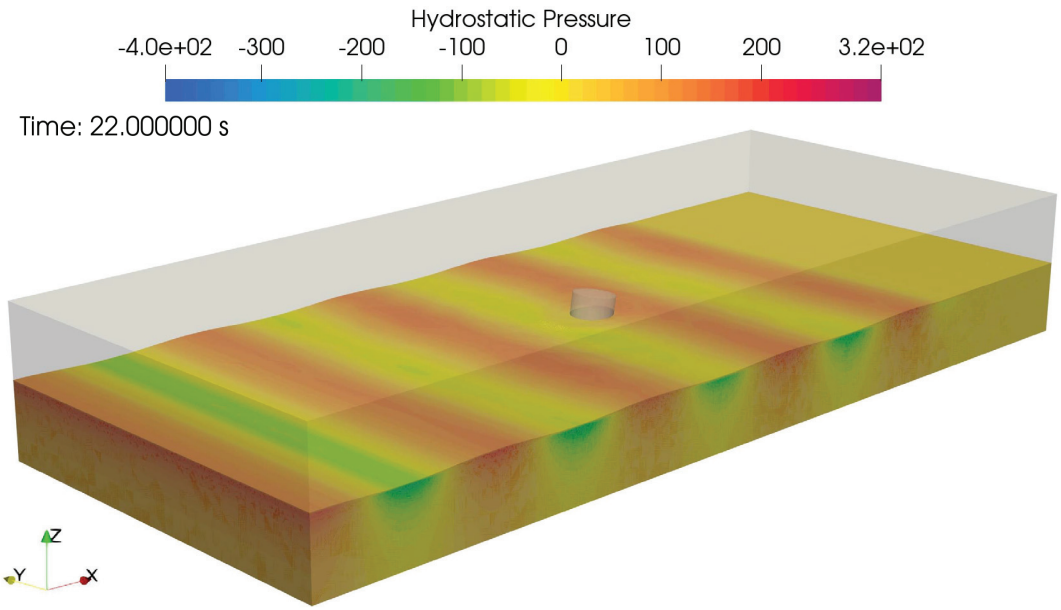

Figure 4.14. Snapshot of hydrostatic pressure representation of entire domain.

The multiphase model, as represented in Figures 4.15 and Figure 4.16 brings out more comprehensively all the dynamics of the system. Where α-water 1 is represented in

red, α-air 0 is represented in blue, and the free surface 0.5 is represented in white.

One can also observe surge displacement, as represented in Figure 4.15, though pitch motion is the primary interest of the study. Mooring lines dominate the restoration of the floater's position with respect to the x-axis. Relaxation zones are also more distinct in the multiphase presentation and allow for better insight into the fluid dynamics.

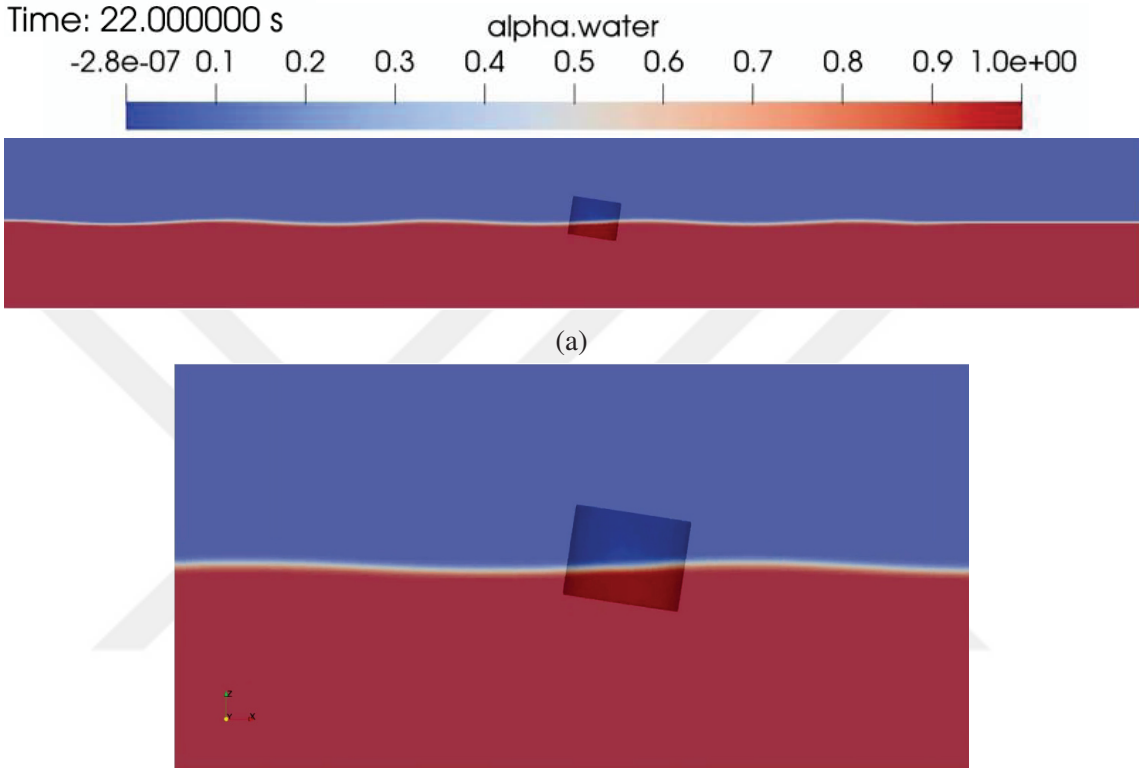

(a)

(b)

Figure 4.15. (a) Entire computational domain showing the moored configuration of the floater with water level representation; (b) Close-up view of the floater with the same water level representation.

In Figure 4.17, the application of the Tuned Liquid Column Damper (TLCD) demonstrates enhanced stability compared to the moored configuration alone, particularly in terms of pitch angle amplitude under regular wave interaction. Between two configurations with TLCD; 37.01% maximum amplitude reduction was achieved. The TLCD-applied scenario achieves a steady amplitude, whereas the solely moored configuration tends to exhibit increasing amplitude as the simulation progresses.

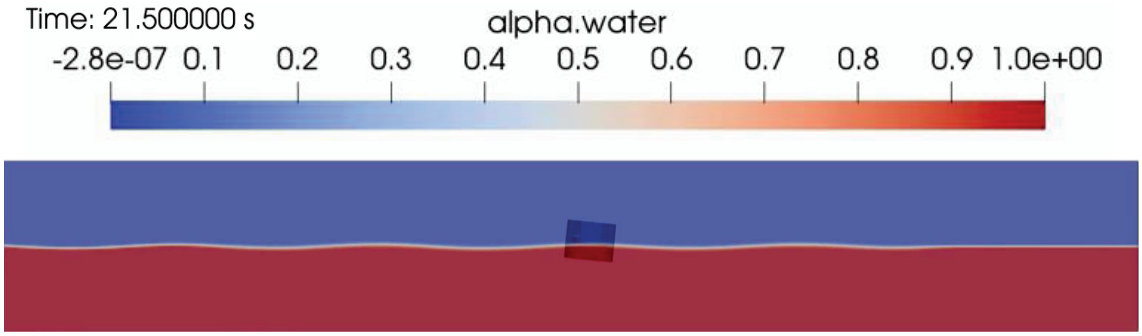

(a)

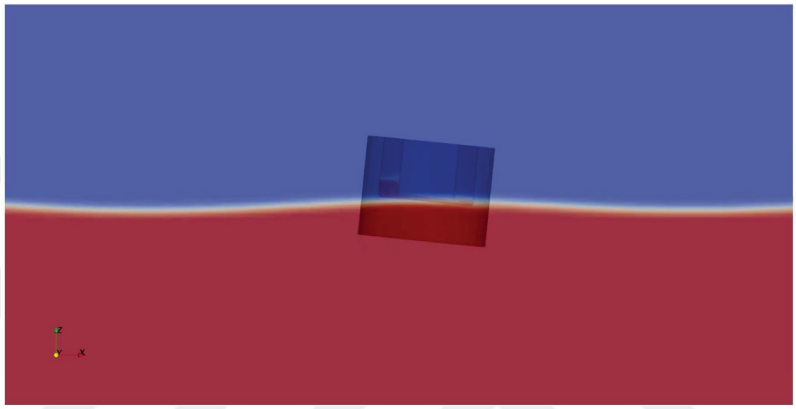

(b)

Figure 4.16. (a) Entire computational domain with 4% TLCD and mooring lines applied; (b) Close-up view of the floater with water level representation.

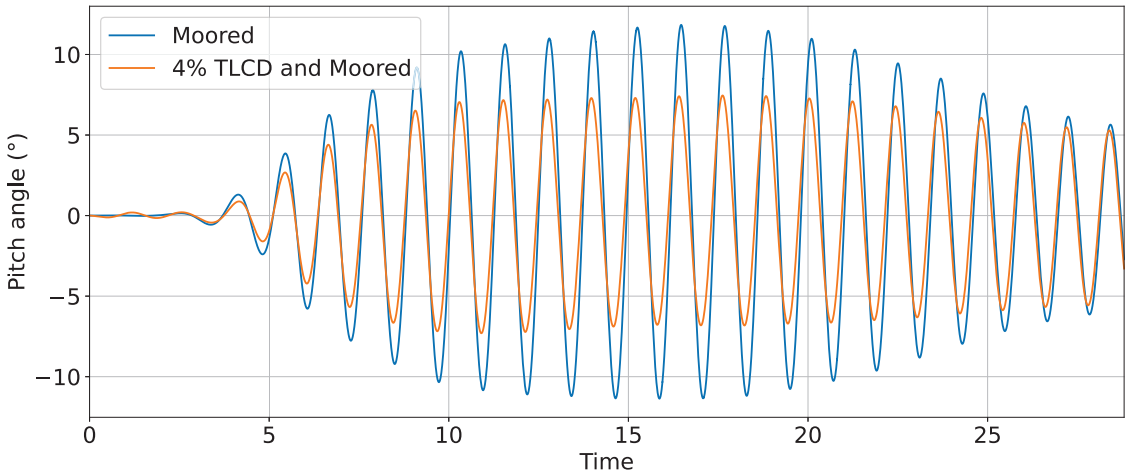

Figure 4.17. Results from comparing the pitch decay motion of the cylindrical floater with base-free configuration, moored and TLCD applied configurations.

CHAPTER 5

CONCLUSIONS

This project aimed to create a high-fidelity, coupled simulation methodology for FOWTs using OpenFOAM, aimed at minimizing undesirable loads and motions by tuned Liquid Column Damper (TLCD).

The developed methodology integrates the waves2Foam (Jacobsen 2017) tool, which leverages the relaxation zone method to generate and absorb wave fields and calculates mooring restraints using a quasi-steady, catenary model. The multiphase simulation employs the waveDyMFoam solver, adapted from the interFoam solver, to execute various dynamic mesh techniques. Utilizing the PIMPLE methodology, the Fluid-Structure Interaction (FSI) coupling incorporates a serial sub-iterating strategy.

The simulation methodology was successfully implemented. Initially, the Anti Roll Tank (ART) system was developed by replicating numerous studies on prescribed motion found in literature, validating its damping performance. This was followed by the replication and validation of free-decay analyses for wave energy converter (WEC) experimental and numerical studies. ART, also known as the Tuned Liquid Column Damper (TLCD), was then applied with 2 different mass ratios of 8% and 4% to WEC to investigate the free-decay motion. Eventually, a coupled simulation of a WEC is possible to implement with this study under combined mooring, a Tuned Liquid Column Damper (TLCD), and wave conditions. Motion mitigation was obtained in free decay condition by 47.80% with a 4% mass ratio TLCD application and 37.01% achieved under regular wave conditions. This shows us promising results this methodology can be successful with FOWTs platforms.

The methodology was able to model very successfully the damping performance of TLMCDs in FOWTs under wave conditions. Thus, the application of this approach to FOWTs can become a sure way for engineers to model TLMCDs. For FOWTs to be designed and operated as efficiently and reliably as possible, it is essential to be able to accurately simulate and evaluate their behaviour under varying operating circumstances.

REFERENCES

Alkarem, Yüksel. 2020. Numerical examination of floating offshore wind turbine and development of an innovative floating platform design. Master's thesis, Izmir Institute of Technology (Turkey).

Ansys, AQWA. 2013. Aqwa theory manual. *AQWA: Canonsburg, PA, USA*.

Arıdıcı, Ali. 2022. Model design and experimental investigation of floating wind turbine. Master's thesis, Izmir Institute of Technology (Turkey).

Arntsen., H. E. Krogstad and Ø. A. 2000. *Linear Wave Theory*. https://folk.ntnu.no/oivarn/hercules_ntnu/LWTcourse/.

Balendra, T, et al. 1999. Vibration control of various types of buildings using tlcd. *Journal of Wind Engineering and Industrial Aerodynamics* 83 (1-3): 197–208.

Berberović, Edin, et al. 2009. Drop impact onto a liquid layer of finite thickness: dynamics of the cavity evolution. *Physical Review E* 79 (3): 036306.

Borg, Michael, et al. 2014. Offshore floating vertical axis wind turbines, dynamics modelling state of the art. part ii: mooring line and structural dynamics. *Renewable and Sustainable Energy Reviews* 39:1226–1234. ISSN: 1364-0321. https://doi.org/https://doi.org/10.1016/j.rser.2014.07.122. https://www.sciencedirect.com/science/article/pii/S1364032114005747.

Bruinsma, N, et al. 2018. Validation and application of a fully nonlinear numerical wave tank for simulating floating offshore wind turbines. *Ocean Engineering* 147:647–658.

Clement, Chima, et al. 2021. Investigation of viscous damping effect on the coupled dynamic response of a hybrid floating platform concept for offshore wind turbines. *Ocean Engineering* 225:108836.

Community, Blender Online. 2018. *Blender - a 3d modelling and rendering package*. Stichting Blender Foundation, Amsterdam: Blender Foundation. http://www.blender.org.

Coudurier, Christophe, et al. 2015. Passive and semi-active control of an offshore floating wind turbine using a tuned liquid column damper. *IFAC-PapersOnLine* 48 (16): 241–247.

Coudurier, Christophe, et al. 2018. Modelling of a tuned liquid multi-column damper. application to floating wind turbine for improved robustness against wave incidence. *Ocean Engineering* 165:277–292.

Cruz, Joao, et al. 2016. *Floating offshore wind energy: the next generation of wind energy.* Springer.

Dean, Robert G. 1965. Stream function wave theory: validity and application. In *Proceedings santa barbara specialty conference.* ASCE.

Decorte, Griet, et al. 2019. A first assessment of the interdependency of mesh motion and free surface models in openfoam regarding wave-structure interaction. In *Marine viii: proceedings of the viii international conference on computational methods in marine engineering,* 795–806. CIMNE.

Delaunay, J. 2012. Numerical simulation of motion stabilization by u-tube anti-roll tanks using cfd. PhD diss., Master's thesis, Universite de Bretagne Occidentale.(a) ers for cell . . .

Doerry, Armin Walter. 2008. *Ship dynamics for maritime isar imaging.* Technical report. Sandia National Laboratories (SNL), Albuquerque, NM, and Livermore, CA . . .

Dunbar, Alexander J, et al. 2015. Development and validation of a tightly coupled cfd/6-dof solver for simulating floating offshore wind turbine platforms. *Ocean Engineering* 110:98–105.

Erlend, Gjelstad. 2021. *Oceans unlocked - a floating wind future* [in en]. Accessed January 6, 2024. https://www.cowi.com/insights/oceans-unlocked-a-floating-wind-future.

Ferziger, Joel H, et al. 2002. *Computational methods for fluid dynamics.* Springer.

Field, SB, et al. 1976. Comparative effects of u-tube and free surface type passive roll stabilisation systems. *Naval Architect,* no. 2.

Frahm, Herr H. 1911. Results of trials of the anti-rolling tanks at sea. *Journal of the American Society for Naval Engineers* 23 (2): 571–597.

Frontera Pericàs, Pere. 2022. Cfd simulation of a floating wind turbine in openfoam: an fsi approach based on the actuator line and relaxation zone methods. Master's thesis, Universitat Politècnica de Catalunya.

Goda, Yoshimi. 2010. *Random seas and design of maritime structures.* Vol. 33. World Scientific Publishing Company.

Greenshields, Christopher. 2023. *Openfoam v11 user guide.* London, UK: The OpenFOAM Foundation. https://doc.cfd.direct/openfoam/user-guide-v11.

Greenshields, Christopher J, et al. 2022. Notes on computational fluid dynamics: general principles. *(No Title).*

Gunsing, Michiel, et al. 2014. Experimental Data on the Systematic Variation of the Internal Damping Inside a U-Shaped Anti-Roll Tank [in en]. In *Volume 7: Ocean Space Utilization; Professor Emeritus J. Randolph Paulling Honoring Symposium on Ocean Technology,* V007T12A013. San Francisco, California, USA: American Society of Mechanical Engineers, June. ISBN: 978-0-7918-4549-3, accessed May 18, 2023. https://doi.org/10.1115/OMAE2014-23799. https://asmedigitalcollection.asme.org/OMAE/proceedings/OMAE2014/45493/San%20Francisco,%20California,%20USA/278518.

GWEC. 2023. *Gwec | global wind report 2023* [in en]. Accessed January 6, 2024. https://gwec.net/wp-content/uploads/2023/03/GWR-2023_interactive.pdf.

Hasselmann, Klaus, et al. 1973. Measurements of wind-wave growth and swell decay during the joint north sea wave project (jonswap). *Ergaenzungsheft zur Deutschen Hydrographischen Zeitschrift, Reihe A.*

Hegseth, John Marius, et al. 2019. A semi-analytical frequency domain model for efficient design evaluation of spar floating wind turbines. *Marine Structures* 64:186–210.

Hemmati, Arash, et al. 2019. Fragility reduction of offshore wind turbines using tuned liquid column dampers. *Soil Dynamics and Earthquake Engineering* 125:105705.

Hirt, Cyril W, et al. 1981. Volume of fluid (vof) method for the dynamics of free boundaries. *Journal of computational physics* 39 (1): 201–225.

Holzmann, Tobias. 2019. *Mathematics, numerics, derivations and openfoam®.* November.

Huang, Yang, et al. 2021. Hydrodynamic study and performance analysis of the oc4-deepcwind platform by cfd method. *International Journal of Computational Methods* 18 (04): 2050020.

Ippen, Arthur T. 1966. Estuary and coastline hydrodynamics. *McGraw-Hill Book Company, IncCatalog Card Number 65-27677, Printed in the United States of America.*

Jacobsen, Niels G. 2017. Waves2foam manual. *Deltares, The Netherlands* 570.

Jacobsen, Niels G, et al. 2012. A wave generation toolbox for the open-source cfd library: openfoam®. *International Journal for numerical methods in fluids* 70 (9): 1073–1088.

Jonkman, Jason, et al. 2010. *Offshore code comparison collaboration (oc3) for iea wind task 23 offshore wind technology and deployment.* Technical report. National Renewable Energy Lab.(NREL), Golden, CO (United States).

Jonkman, Jason Mark, et al. 2005. *Fast user's guide-updated august 2005.* Technical report. National Renewable Energy Lab.(NREL), Golden, CO (United States).

Karimi, Meysam, et al. 2017. A multi-objective design optimization approach for floating offshore wind turbine support structures. *Journal of Ocean Engineering and Marine Energy* 3:69–87.

Kerkvliet, Maarten, et al. 2014. Analysis of u-type anti-roll tank using urans: sensitivity and validation. In *International conference on offshore mechanics and arctic engineering,* vol. 45400, V002T08A031. American Society of Mechanical Engineers.

Liu, Yuanchuan, et al. 2017. Establishing a fully coupled cfd analysis tool for floating offshore wind turbines. *Renewable Energy* 112:280–301. ISSN: 0960-1481. https://doi.org/https://doi.org/10.1016/j.renene.2017.04.052. https://www.sciencedirect.com/science/article/pii/S0960148117303609.

Luo, Ningsu, et al. 2011. Semiactive control for floating offshore wind turbines subject to aero-hydro dynamic loads. In *International conference on renewable energies and power quality.*

Menter, Florian R. 1994. Two-equation eddy-viscosity turbulence models for engineering applications. *AIAA journal* 32 (8): 1598–1605.

Moaleji, Reza, et al. 2007. On the development of ship anti-roll tanks. *Ocean Engineering* 34 (1): 103–121.

Molland, Anthony F., ed. 2008. Chapter 7 - seakeeping. In *The maritime engineering reference book,* 483–577. Oxford: Butterworth-Heinemann. ISBN: 978-0-7506-8987-8. https://doi.org/https://doi.org/10.1016/B978-0-7506-8987-8.00007-X. https://www.sciencedirect.com/science/article/pii/B978075068987800007X.

Moukalled, Fadl, et al. 2016. *The finite volume method.* Springer.

Munk, Walter Heinrich. 1951. *Origin and generation of waves.* Scripps Institution of Oceanography La Jolla, California.

Newman, John Nicholas. 2018. *Marine hydrodynamics.* The MIT press.

OpenFOAM – CFD Online Discussion Forums. 2024. https://www.cfd-online.com/Forums/openfoam/.

Otter, Aldert, et al. 2022. A review of modelling techniques for floating offshore wind turbines [in en]. Number: 5, *Wind Energy* 25, no. 5 (May): 831–857. ISSN: 1095-4244, 1099-1824, accessed May 18, 2023. https://doi.org/10.1002/we.2701. https://onlinelibrary.wiley.com/doi/10.1002/we.2701.

Palm, Johannes, et al. 2016. Coupled mooring analysis for floating wave energy converters using cfd: formulation and validation. *International Journal of Marine Energy* 16:83–99.

Paredes, Guilherme Moura, et al. 2015. Experimental investigation of mooring configurations for wave energy converters. *Resonance* 60 (80): 100.

Pegalajar-Jurado, Antonio, et al. 2018. An efficient frequency-domain model for quick load analysis of floating offshore wind turbines. *Wind Energy Science* 3 (2): 693–712.

Prosperetti, Andrea, et al. 2009. *Computational methods for multiphase flow*. Cambridge university press.

Rainey, RCT. 2007. Weak or strong nonlinearity: the vital issue. *Journal of Engineering Mathematics* 58:229–249.

Rivera-Arreba, Irene, et al. 2018. Modeling of a semisubmersible floating wind platform in severe waves. In *International conference on offshore mechanics and arctic engineering,* vol. 51302, V009T13A002. American Society of Mechanical Engineers.

Robertson, Amu N, et al. 2020. Oc6 phase i: investigating the underprediction of low-frequency hydrodynamic loads and responses of a floating wind turbine. In *Journal of physics: conference series,* 1618:032033. 3. IOP Publishing.

Robertson, Amy, et al. 2014. Offshore code comparison collaboration continuation within iea wind task 30: phase ii results regarding a floating semisubmersible wind system. In *International conference on offshore mechanics and arctic engineering,* vol. 45547, V09BT09A012. American Society of Mechanical Engineers.

Robertson, Amy N, et al. 2017. Oc5 project phase ii: validation of global loads of the deepcwind floating semisubmersible wind turbine. *Energy Procedia* 137:38–57.

Robertson, AN, et al. 2011. Loads analysis of several offshore floating wind turbine concepts. *Contract.*

Rodriguez Marijuan, Alberto. 2017. *Offshore floating platforms: analysis of a solution for motion mitigation.*

Saaed, Tarek Edrees, et al. 2013. A state-of-the-art review of structural control systems. *Journal of Vibration and Control* 21 (5): 919–937.

Sabatier, François. 2007. Us army corps of engineers, coastal engineering manual (cem), engineer manual 1110-2-1100. *Méditerranée,* no. 108, 146.

Sarpkaya, Turgut. 2010. *Wave forces on offshore structures.* Cambridge university press.

Schmitt, Pál, et al. 2020. Beyond vof: alternative openfoam solvers for numerical wave tanks. *Journal of ocean engineering and marine energy* 6:277–292.

Shadman, Milad, et al. 2012. Utilizing tlcd (tuned liquid column damper) in floating wind turbines. In *International conference on offshore mechanics and arctic engineering,* 44946:241–247. American Society of Mechanical Engineers.

Thanyamanta, Worakanok, et al. 2012. Prediction of stabilizing moments and effects of u-tube anti-roll tank geometry using cfd. In *International conference on offshore mechanics and arctic engineering,* 44922:503–512. American Society of Mechanical Engineers.

The official user tutorials and programmer's guides [in en]. 2024. https://www.openfoam.com/documentation/overview.

Tran, Thanh Toan, et al. 2016. Fully coupled aero-hydrodynamic analysis of a semi-submersible fowt using a dynamic fluid body interaction approach. *Renewable energy* 92:244–261.

Tutorial Guide [in en]. 2024. https://www.openfoam.com/documentation/tutorial-guide.

Wang, Lu, et al. 2022. Oc6 phase ia: cfd simulations of the free-decay motion of the deepcwind semisubmersible. *Energies* 15 (1): 389.

Windt, Christian, et al. 2018. Performance assessment of the overset grid method for numerical wave tank experiments in the openfoam environment. In *International conference on offshore mechanics and arctic engineering,* vol. 51319, V010T09A006. American Society of Mechanical Engineers.

Windt, Christian, et al. 2020. Evaluation of the overset grid method for control studies of wave energy converters in openfoam numerical wave tanks. *Journal of Ocean Engineering and Marine Energy* 6 (1): 55–70.

Xue, Mi-An, et al. 2022. Pitch motion reduction of semisubmersible floating offshore wind turbine substructure using a tuned liquid multicolumn damper. *Marine Structures* 84:103237.

Zhou, Yang, et al. 2022. Investigations on the effects of internal liquid sloshing of semi-submersible floating offshore wind turbines. In *International conference on offshore mechanics and arctic engineering,* vol. 85857, V001T01A024. American Society of Mechanical Engineers.

Zhou, Yang, et al. 2023. Sloshing dynamics of a tuned liquid multi-column damper for semi-submersible floating offshore wind turbines. *Ocean Engineering* 269:113484.